



Resolving indoor shortwave and longwave human body irradiance variations for mean radiant temperature and local thermal comfort

Miaomiao Hou^{b,d,1}, Dorit Aviv^{b,1}, Arnab Chatterjee^a, Eric Teitelbaum^c, Mohamad Rida^a, Forrest Meggers^c, Dolaana Khovalyg^{a,*}

^a Laboratory of Integrated Comfort Engineering (ICE), École Polytechnique fédérale de Lausanne (EPFL), CH, Fribourg 1700, Switzerland

^b Weitzman School of Design, University of Pennsylvania, Philadelphia, 19104, PA, United States

^c Cooling and Heating for Architecturally Optimized Systems (CHAOS) Lab, Andlinger Center for Energy and the Environment, Princeton University, Princeton, 08544, NJ, United States

^d College of Architecture and Urban Planning, Tongji University, Shanghai 200092, China

ARTICLE INFO

Keywords:

Mean radiant temperature
Radiant heat transfer
Local thermal comfort
Ray tracing
Irradiance
Human body
Simulation

ABSTRACT

A spatially and directionally resolved longwave and shortwave radiant heat transfer model is presented via a series of experiments in a thermal lab to input surface temperatures and geometries, as well as skin temperature readings from a human subject, in order to test mean radiant temperature (MRT) and thermal comfort results for the person. Combining novel scanning and thermography methods together with ray-tracing simulation, high-resolution thermal models are derived fully characterizing the longwave and shortwave radiant heat fluxes in space and resolving the impact of these variations on MRT. The study demonstrates the significant amount of spatial variation of both shortwave and longwave radiant heat transfer on MRT through the room and also across body segments: the experimental results show variations of up to 14.5 °C across the room, leading to PMV comfort variations from −0.27 to 2.45, clearly demonstrating the importance of mapping the entire radiant field rather than assuming one MRT value for a thermal zone. Furthermore, local radiant temperature, newly defined Body Segment Plane Radiant Temperature (BSPRT), variations across the body of more than 30 °C are found. Finally, a detailed human thermo-physiology model was used to evaluate the possible variation in thermal sensation between the different body segments due to the large differences in local MRT.

1. Introduction

1.1. Radiant heat exchange and thermal comfort

While thermal comfort is defined as “condition of the mind in which satisfaction is expressed with the thermal environment” [1], about half of the heat exchange between the human body and the environment that determines thermal comfort is due to radiant heat transfer [2]. The radiant heat exchanges between the human body and the surroundings can be split into solar (shortwave) radiation and longwave radiation from all the surrounding surfaces. The presence of solar radiation or heat sources within a space can cause heterogeneous shortwave or longwave irradiance fields, respectively, resulting in a transient-changing or spatially non-uniform thermal environment. Although the thermal comfort of occupants can be directly affected by shortwave radiation,

not many studies have addressed the impacts of shortwave radiation on thermal comfort until recent years [3–5]. The shortwave radiation has been added to the ASHRAE Standard 55 only starting the 2017 version [6]. A thermally asymmetrical environment has the potential to be more comfortable than the usual optimum of uniformity, and the occupant’s thermal sensation and comfort of local body segments need to be considered in determining the overall comfort effects [7].

In order to analyze local differences between body segments, Kaynakli et al. [8] investigated the human thermal comfort model for sitting and standing posture, evaluating the difference in heat loss rather than radiant temperature between individual body segments. Sorensen [9] calculated the view factors between the individual of the 16 body segments and between the body segments and the outer surfaces by using a thermal manikin, revealing that radiation between individual body segments could be important for thermal comfort. Atmaca et al. [10] used a numerical model of the view factor method to calculate the

* Corresponding author.

E-mail address: dolaana.khovalyg@epfl.ch (D. Khovalyg).

¹ First authors.

Nomenclature

A_i	Area of the i^{th} body segment [m^2]		
A	Total body surface area [m^2]		
a_l	Absorption coefficient for longwave radiant flux density [-]		
a_k	Absorption coefficient for shortwave radiant flux density [-]		
$C_1 - C_3$	Regression coefficients for slope of logistic curve [-]		
D	Factor for effect of mean skin temperature on local thermal sensation [-]		
E_r	Total radiated power of a body segment [W/m^2]		
$E_{p\text{ont}}$	Mean spherical irradiance of a point within a space [W/m^2]		
$E_{p\text{ont},lw}$	Longwave mean spherical irradiance of a point within a space [W/m^2]		
$E_{p\text{ont},sw}$	Shortwave mean spherical irradiance of a point within a space [W/m^2]		
K_i	Shortwave heat fluxes in the i direction (up, down, left, right, front, back) [$^\circ C$]		
L_i	Longwave heat fluxes in the i direction (up, down, left, right, front, back) [$^\circ C$]		
MRT_{body}	Mean Radiant Temperature for the entire body with body temperature as inputs [$^\circ C$]		
MRX_{body}	Mean Radiant Heat Flux for the entire body with body temperature as inputs [W/m^2]		
$MRT_{body,lw}$	Longwave portion of Mean Radiant Temperature for the entire body with body temperature as inputs [$^\circ C$]		
$MRX_{body,lw}$	Longwave portion of Mean Radiant Heat Flux for the entire body with body temperature as inputs [W/m^2]		
$MRX_{body,sw}$	Shortwave portion of Mean Radiant Heat Flux for the entire body with body temperature as inputs [W/m^2]		
MRT_{bd-no}	Mean Radiant Temperature for the entire body without body temperature as inputs [$^\circ C$]		
MRT_{point}	Mean Radiant Temperature of a point within a space [$^\circ C$]		
MRX_{point}	Mean Radiant Heat Flux of a point within a space [W/m^2]		
$MRT_{point,lw}$	Longwave portion of Mean Radiant Temperature of a point within a space [$^\circ C$]		
$MRX_{point,lw}$	Longwave portion of Mean Radiant Heat Flux of a point within a space [W/m^2]		
$MRX_{point,sw}$	Shortwave portion of Mean Radiant Heat Flux of a point within a space [W/m^2]		
$MRT_{3\text{points}}$	A weighted Mean Radiant Temperature from three points representing a sitting person [$^\circ C$]		
MRT_{plane}	Mean Radiant Temperature calculated from the plane		radiant temperature in six directions [$^\circ C$]
		$PD_{warm\text{ceiling}}$	Percentage dissatisfied when radiant asymmetry is caused by a warm ceiling [%]
		$PD_{cool\text{ceiling}}$	Percentage dissatisfied when radiant asymmetry is caused by a cool ceiling [%]
		$PD_{warm\text{wall}}$	Percentage dissatisfied when radiant asymmetry is caused by a warm wall [%]
		$PD_{cool\text{wall}}$	Percentage dissatisfied when radiant asymmetry is caused by a cool wall [%]
		PMV_{body}	Predicted Mean Vote (PMV) from whole-body MRT MRT_{body} [-]
		$PMV_{body-no}$	Predicted Mean Vote (PMV) from whole-body MRT without body temperature as inputs $MRT_{body-no}$ [-]
		PMV_{point}	Predicted Mean Vote (PMV) from point-based MRT MRT_{point} [-]
		$PMV_{3\text{points}}$	Predicted Mean Vote (PMV) from $MRT_{3\text{points}}$ [-]
		PMV_{plane}	Predicted Mean Vote (PMV) from MRT calculated by the plane method MRT_{plane} [-]
		S_i	Thermal sensation of the i^{th} body segment [9 points scale]
		T_r	Body Segment Plane Radiant Temperature (BSPRT) [$^\circ C$]
		$BSPRX$	Body Segment Plane Radiant Heat Flux [W/m^2]
		$T_{r,i}$	Body Segment Plane Radiant Temperature (BSPRT) of the i^{th} body segment [$^\circ C$]
		$T_{r,lw}$	Longwave Body Segment Plane Radiant Temperature [$^\circ C$]
		$BSPRX_{r,lw}$	Longwave Body Segment Plane Radiant Heat Flux [W/m^2]
		$T_{r,lw,i}$	Longwave Body Segment Plane Radiant Temperature of the i^{th} body segment [$^\circ C$]
		$T_{r,sw}$	Shortwave Body Segment Plane Radiant Temperature [$^\circ C$]
		$BSPRX_{r,sw}$	Shortwave Body Segment Plane Radiant Heat Flux [W/m^2]
		$T_{r,sw,i}$	Shortwave Body Segment Plane Radiant Temperature of the i^{th} body segment [$^\circ C$]
		$T_{skin,i}$	Skin temperature of the i^{th} body segment [$^\circ C$]
		$T_{skin,mean}$	Mean skin temperature [$^\circ C$]
		T_{core}	Core temperature [$^\circ C$]
		$T_{set,skin,i}$	Set point skin temperature of the i^{th} body segment [$^\circ C$]
		$T_{set,skin,mean}$	Mean set point skin temperature [$^\circ C$]
		$t_{p,i}$	Plane radiant temperature in the i direction (up, down, left, right, front, back) [$^\circ C$]
		Δt_{pr}	Radiant temperature asymmetry [$^\circ C$]
		σ	Stefan-Boltzman constant as 5.67×10^{-8} [W/m^2K^4]

radiant temperature for each of the 16 body segments and its impact on Predicted Mean Vote (PMV) index. Even though the impacts of radiant temperature on the overall PMV have been investigated, the radiant heterogeneity and asymmetry need more clarification at a high-resolution level considering the complicated geometry of the human body and the environment. The real thermal environments for human's daily life are often non-uniform and radiant heterogeneous. It has been shown that local thermal sensation has a large impact on the whole body's thermal comfort [7]. As a result, more and more recent approaches to predict comfort based on thermal responses of local body parts have been developed, including thermo-physiological models and thermal sensation models. The thermo-physiological model (e.g., Fiala's model, Tanabe's model JOS3, ThermoSEM model) can be used to calculate the core and skin temperature [11], and these outputs can be input to thermal sensation models to predict local thermal comfort. Besides human physiological inputs, environmental parameters, including mean radiant temperature (MRT), are also needed for each

body segment; in addition, the view factor between the segment and the surrounding environment is still difficult to estimate.

1.2. MRT measurements

The mean radiant temperature (MRT) is defined as *the uniform temperature of an imaginary enclosure in which radiative heat transfer from the human body is equal to the radiative heat transfer in the actual non-uniform enclosure* according to the ASHRAE standard 55 [1]. MRT has been used in comfort models to represent the impacts of all radiant heat fluxes reaching the body including the Predicted Mean Vote (PMV) model by Fanger [12,13]. In the indoor environment, MRT is often calculated as a homogeneous environmental parameter per a given space. Considering the extensive geometric complexity involved, simplifications of the human body to different degrees from a single point to solid segments were used in the literature [14–16]. The calculation methods and representation of MRT in experimental work, largely depend on the ability

to measure this variable. Measurement methods can be categorized into three types: a point or a sphere measurement when using a black globe thermometer; plane radiant temperature, when using radiometers; or calculation of view factors based on temperature measurements of the surrounding surfaces. When MRT is measured by a black globe thermometer, its value can be estimated to be equivalent to the mean spherical irradiance received by a black sphere at the test point. However, the globe thermometer, the most commonly used device to derive MRT, has a systematic error in its use baked into the standards that describe its deployment and MRT derivation [17–19]. MRT can also be measured by sensing the plane radiant temperature in six directions, weighted according to the projected area factors for the occupant [20]. The plane radiant temperature is defined as *the uniform temperature of an enclosure where the irradiance on one side of a small plane element is the same as in the actual non-uniform environment* [21]. When radiation comes from different directions within the space with appreciable thermal heterogeneities, MRT alone cannot fully characterize the radiative environment [22]. In cases where different heat sources are present, including solar impact, *radiant asymmetry* can be used to evaluate the effect of the asymmetric radiant field on thermal comfort [23]. The recent growth of cross-pollination work in biometeorology and building science has led to works developing methods for better characterizing radiant environments such as Middel et al. [24,25] and Lee et al. [26,27] producing new hybrid uses of shortwave sensors with thermal imaging devices. Furthermore, Merchant et al. [28] and Aviv et al. [29] have developed sensors and models to translate surface temperature data into a volumetric analysis of variation potential radiant heat transfer and MRT throughout space using novel ray tracing methods presented in Aviv et al. [30–32].

1.3. MRT simulation techniques

There are several computational tools that can be used for MRT simulation. The ability to calibrate MRT simulation methods is only as accurate and precise as one's ability to measure it, a fundamental issue with this abstract quantity. For the indoor environment, several common tools can simulate indoor MRT with surface temperatures using view factors. The surface temperatures can be derived either from energy simulations, such as in TRNSYS and EnergyPlus, or from direct inputs by users in some cases, such as CBE's MRT Calculator [33]. However, these tools for indoor MRT seldom account for the shortwave radiant heat fluxes. What's more, the body geometry is simplified into a point or a box scaled by projected area factors without detailed representation. To evaluate the thermal radiant field induced by the presence of shortwave radiation, several models for MRT calculation use the projected area of a standard person exposed to direct beam sunlight to characterize the geometric relationship between the human body and the environment, such as a generalized algorithm proposed by La Genuza et al. [34] and SolarCal [35]. It aims to provide quick and interactive results with the simplification of room and body geometries and predefined reflectivities of room materials that cannot be modified. In contrast, the simulation tools for outdoor MRT include the shortwave component and a more detailed body geometry [22]. For instance, Ladybug/Honeybee environmental analysis plugins use EnergyPlus as the engine to account for the longwave radiation, and the shortwave component is simulated with a mannequin model composed of 482 meshes. The detailed body model is not used for the longwave component and the reflected longwave radiation is also neglected in this tool. CFD software accounts for all forms of heat transfer including thermal radiation and can provide accurate results for complex geometries [36–38], but this tool is generally computationally demanding in time and cost.

1.4. Scope of the study

Existing studies have combined the impacts of shortwave and

longwave radiation on thermal comfort and provided tools for quick MRT estimation. However, the spatial resolution of MRT reveals only the whole-body thermal comfort effects instead of the irradiance variations across the body. Likewise, previous studies did not take the detailed room geometry and reflectivities of all exposed surfaces or the complete variations of shortwave radiation from the morning to the sunset into account. Our aim is to validate a heat transfer simulation framework that evaluates spatial and spectral variation in thermal radiation that addresses gaps and simplifications existing in the empirical analysis of human comfort response. We further advance methods developed in [28–32,39] and propose added specificity to radiant terms to address variations in shortwave and longwave thermal radiation along with their spatial variation at the scale of the body. We deploy a novel sensor suite to measure the longwave and shortwave environments to create a high-resolution thermal input for a human body segment MRT simulation. The ray-tracing simulation combined with novel scanning and thermography methods are used to calculate both the shortwave and longwave irradiance falling onto an imaginary sphere or a body segment within a space. Sensor data from wearable sensors by a human subject and various environmental sensors provide information on both the room surface temperature variation and the human skin temperature at different measurement points. This detailed analysis across multiple wavelengths, including longwave multi-bounces, is novel in the field and it addresses systematic gaps in spatial resolution of current methodologies. This work aims to present the functionality of these new methods with an initial case study and preliminary comparison with other methods and demonstrates the challenges and required future work in validating both current and our proposed new methods for characterizations of radiant heat exchanges in the built environment.

To characterize the radiative heat exchanges between the human body and the environment, the plane radiant temperature of each body segment can be calculated, and the mean of those would yield MRT. We define the plane radiant temperature for each segment of a body surface as a Body Segment Plane Radiant Temperature (BSPRT). Therefore, BSPRT is *the uniform temperature of an enclosure where the irradiance of the exposed side of a small plane element on a body segment is the same as in the actual non-uniform environment* (Fig. 1). The MRT of the full body can be considered equal to the mean BSPRT of all body segments, weighted by the surface area of the segments. Thus, the first aim of this study is to quantify how significant the spatial variation of MRT and PMV through the room and also BSPRT across body segments would be. The second aim is to provide a validated model that can characterize the irradiation on a full geometric model of the body, considering the influence of self-occlusion and body temperature. The third aim is to demonstrate the potential influence of the local MRT variability on the local thermal sensation using the human thermo-physiology model (HTPM) coupled with the local thermal sensation and comfort model. Practically, increasing the level of input for HTPM to include local MRT will improve the accuracy of the local skin temperatures and thermal sensation prediction.

2. Methods

In the following sections we present our proposed novel methodological workflow connecting high spatial and thermal resolution experimental data in a controlled experimental office space with radiant ceiling panels, windows, and a human occupant, to a data-driven ray-tracing simulation to calculate local body temperature and overall MRT. We apply the results to a thermophysiological model to determine the potential variation in local thermal sensation due to the Body Segment Plane Radiant Temperature (BSPRT) variation.

2.1. Experimental setup

2.1.1. Facility

A single-story office building prototype, a shared research facility of Smart Living Lab in Fribourg, Switzerland, is used to perform

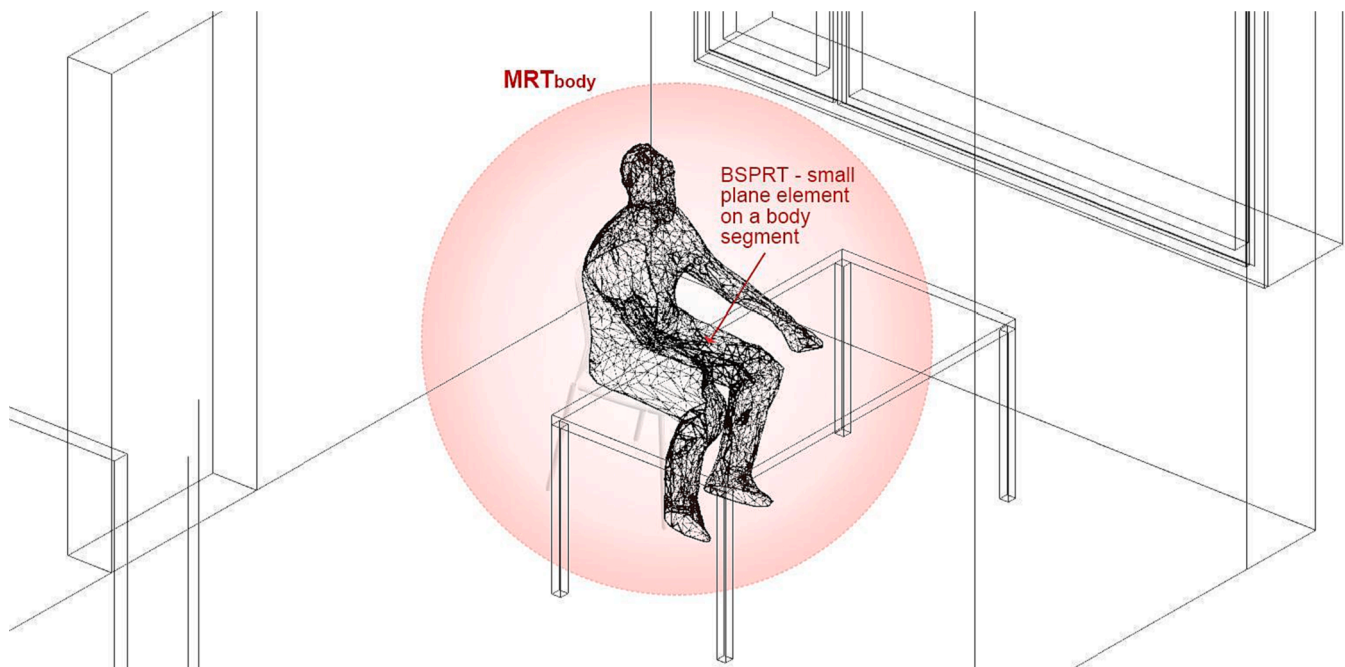


Fig. 1. Diagram of the MRT of the whole body and of a Body Segment Plane Radiant Temperature (BSPRT) of a surface on the left anterior thigh.

experiments. Detailed description of the facility is provided in [40]. The facility has two nearly identical rooms, and the West room was chosen for experimentation. The floor area of the room is 19 m^2 , and the height is 3.1 m. There are two 4.6 m^2 windows, one facing South and another one facing North (Fig. 2a). The windows are double-glazed with a g-value 65 %, and average transmittance of 36 % over 285–3000 nm. Each window is equipped with an internal textile roller blind (35 cm inward from the window frame) and an external Venetian blind. For thermal conditioning, the room is equipped with a radiant ceiling with 3 panels 0.31 m apart from each other (Fig. 2b). The overall surface area of the panels is $0.33 \text{ m} \times 3.75 \text{ m}$, and their position is offset towards the North-West. Fresh air is supplied through a circular wall diffuser of 100 mm with slats located 2.83 m above the floor and 1.5 m away from the North internal wall. An air exhaust vent of the same size as the supply locates 0.4 m above the floor and 1.59 m away from the South internal wall. Ventilation is balanced, and the extraction flow rate is equal to the supply flow rate. The supply flow rate of fresh air is $68.5 \text{ m}^3/\text{h}$ (1.15 ACH), the minimum required for the proper operation of the ventilation unit, and the ventilation works through ON-OFF cycles of 15 min each.

The room has two 5 m-long strip lights. One ceiling light is located between two radiant panels, and the other one is 1.87 m away from the first one. In terms of the furniture, there was only a desk placed 50 cm from the South wall and an office chair.

2.1.2. Experimental cases

The overview of experimental cases is provided in Table 1 and Fig. 4. In all experiments, the blinds of the North window were down. The blinds of the South window, internal textile, and external Venetian, were UP in experiments I and II (Fig. 4a,b) and DOWN in experiment III (Fig. 4c). In experiment I, there were three 0.5 m-wide strips of reflective aluminum cover floor to ceiling, as shown in Fig. 4(a) on the West wall that is directly exposed to the Sun in the mornings (0.5 m inward from the South wall). The purpose was to explore the effect of the reflective surface on the local radiant environment. In each experimental case I-III, the measurements were conducted in two different configurations; one with the human subject seated inside the room (OCC) which lasted for 90 min, and it was followed by further measurements for 30 min in the absence of the human subject (UNOC). In each of the above

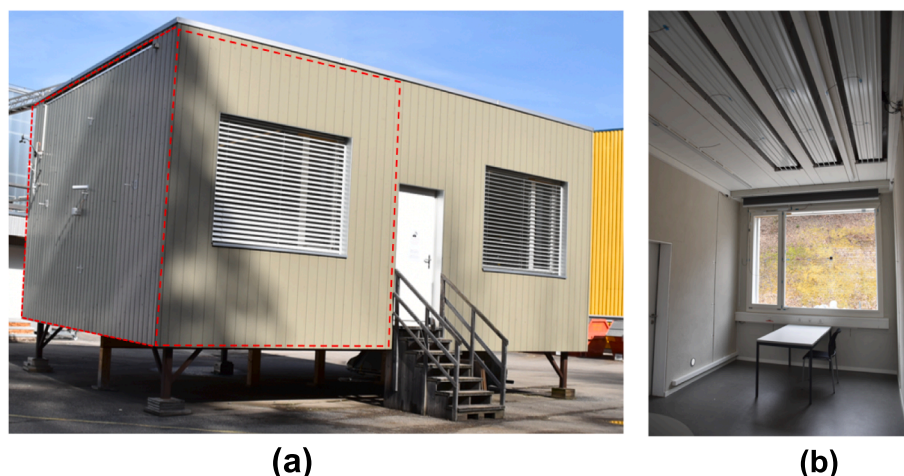


Fig. 2. Overview of the experimental facility: (a) outside view (West room used for experimentation is highlighted), (b) indoors (South-facing view).

Table 1
Overview of experimental cases and conditions.

Parameters	Experiment I (South blinds Up+ Reflective strip)			Experiment II (South blinds UP)			Experiment III (South blinds DOWN)			
	a (OCC)	b (OCC)	c (UNOC)	a (OCC)	b (OCC)	c (UNOC)	a (OCC)	b (OCC)	c (UNOC)	
Experimental cases	a	b	c	a	b	c	a	b	c	
Timing of SMART scanning sequence	10:17–10:47	10:52–11:22	11:35–12:11	13:12–13:42	13:47–14:17	14:36–15:06	15:34–16:04	16:15–16:45	17:01–17:31	
Reflective Surface	Yes			No			No			
South Blinds	External	Up			Up			Down		
	Internal	Up			Up			Down		
Person Occupancy	Yes	Yes	No	Yes	Yes	No	Yes	Yes	No	

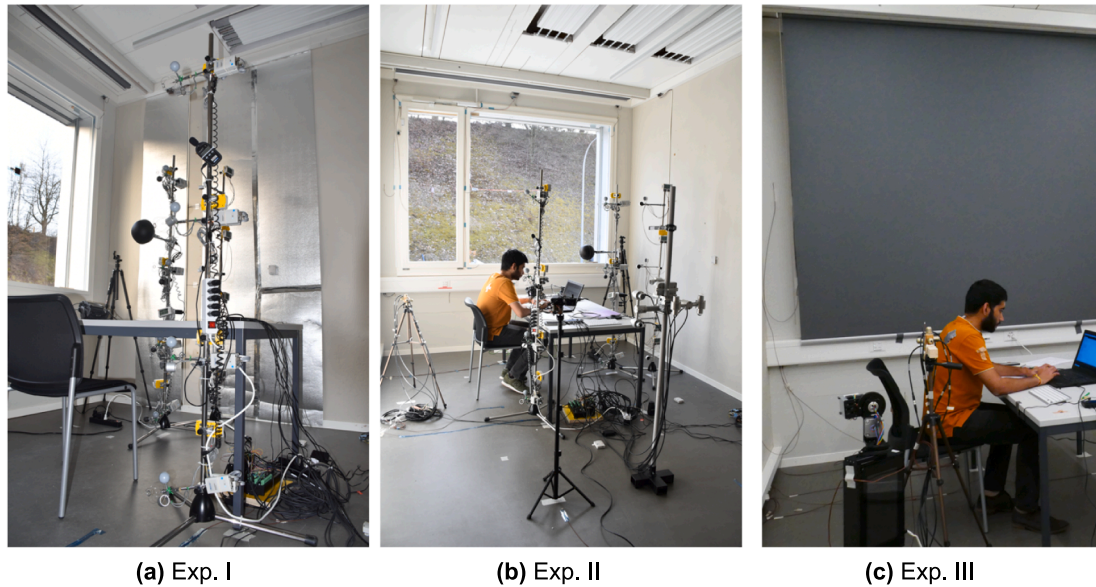


Fig. 4. Overview of experimental arrangements: (a) Experiment I (with reflective strips on the West wall), (b) Experiment II (with no reflective strips), (c) Experiment III (South-facing window blocked with blinds).

measurement durations, the room was scanned every 30–35 min with the SMART sensor. Both the 6-directional pyrgeometer devices were always recorded during the entire time period of the measurement. The subject also completed a survey every 10 min with questions regarding the overall and local thermal comfort. Other sensors such as thermocouples, iButtons, and anemometers were made to start recording at the beginning of the day, before the start of experiments. The thermal image sequences of indoor surfaces were taken for about 5 min at the end of each experimental case. During the seated period, the subject was performing light seated work. A male participant (28 y.o., BMI = 24 kg/m²) wore a short-sleeve T-shirt, denim pants, sneakers, ankle socks, and underwear resulting in clothing insulation of 0.57 clo. A participant, every 15 minutes from the onset of the experimental cases, completed a survey with questions related to the perceived thermal environment, thermal acceptability, thermal preference, overall thermal sensation, and local thermal discomfort. The study received approval from the EPFL Human Research Ethics Committee (HREC No. 054-2020).

2.1.3. Sensors

Two groups of sensors were used in the study, environmental sensors (indoor and outdoor) and wearable sensors.

(a) Environmental sensing:

Outdoor direct normal and diffuse horizontal irradiance was measured using the SPN1 pyranometer (Delta-T, UK). The accuracy of the instrument was $\pm 10 \text{ W/m}^2$ for individual readings, measurements

were taken every 2 min. To calibrate the shortwave component of the model, hemispherical illuminance (range 1–3000 lm/ft²) was measured using sensors HOBO U12 (Onset, USA) placed at seven different locations indoors.

Two digital, non-contacting longwave measurement devices were used to increase the accuracy of radiant temperature measurements. Primarily, the Scanning Mean Radiant Temperature (SMART) Sensor (Fig. 3a), which is a spatially resolved thermal imager comprised of a Melexis 90,614 five degree field of view non-contacting medical-grade surface temperature sensor (accuracy $\pm 0.5 \text{ }^\circ\text{C}$) and Garmin LidarLite module ($\pm 2 \text{ cm}$ over 40 m) [41]. The sensor rotates on perpendicular axes and records the angular position of the servos, which, combined with Lidar and temperature data, are reconstructed to produce a thermal point cloud of the surface temperatures in the scanned environment. The sensor is placed in a position to avoid occlusion from interior surfaces and occupants as best and possible, and, when a large interior surface causes significant occlusion, multiple point cloud scans can be merged. Additionally, two precision pyrgeometer arrays were used to precisely capture the radiant flux at a point. These devices each were 6 apogee SL-510-SS pyrgeometers ($\pm 0.3 \text{ K}$; $\pm 2 \text{ W/m}^2$) positioned on each surface of a 4 cm cube (Fig. 3b). The temperature recorded by each pyrgeometer was recorded, in addition to the longwave radiant flux in each hemisphere. These are referred to as 6-directional pyrgeometers.

To aid calibration of the model, temperatures of indoor surfaces were captured using an infrared camera FLIR T1030sc (FLIR, USA) between SMART sensor scans. Its spectral range is 7.5–14 μm , the resolution is 1024x768, and the accuracy is within $\pm 1 \text{ }^\circ\text{C}$. Since the IR-camera was

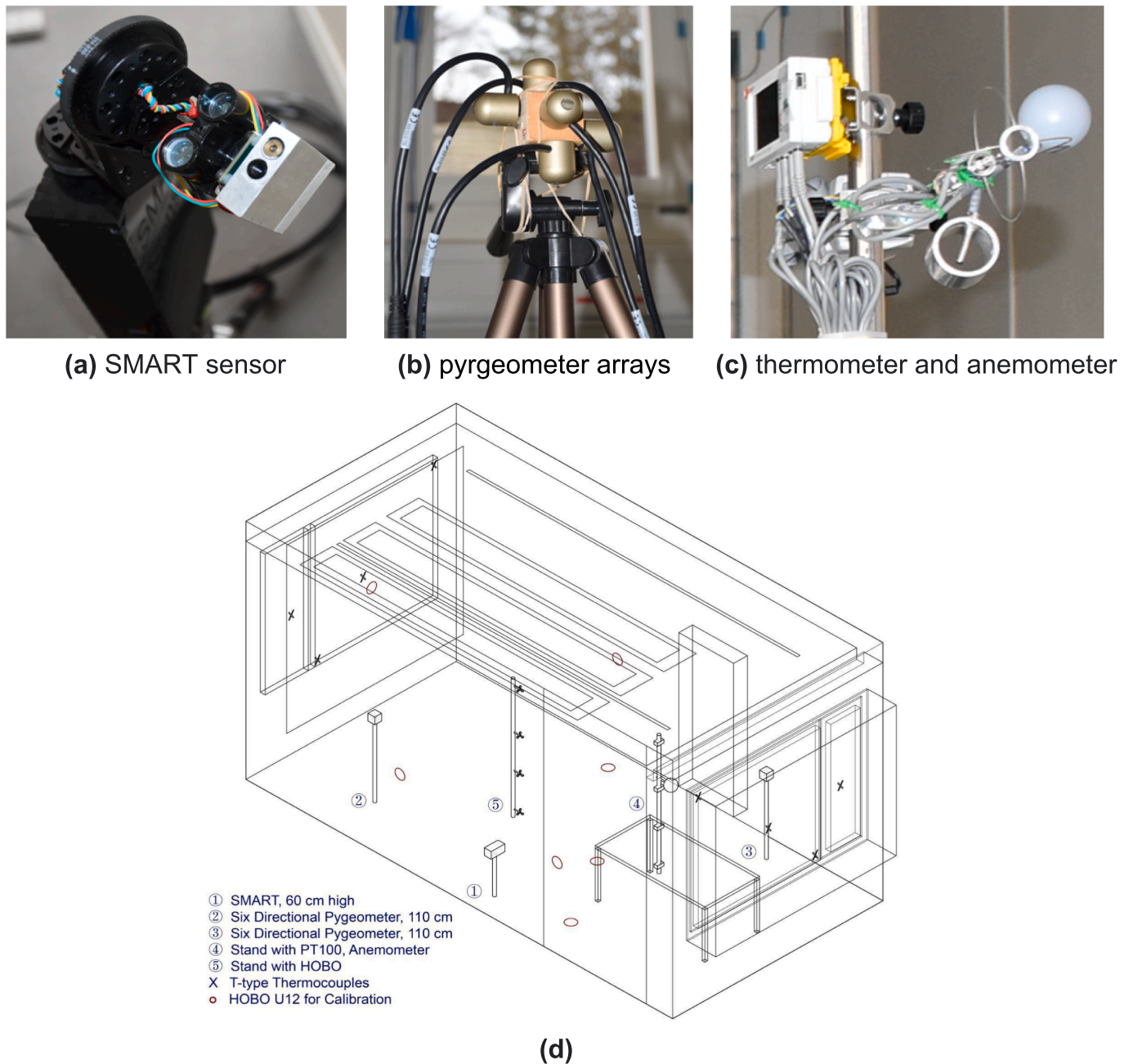


Fig. 3. Overview of the sensors (a-c) and their layout in the experimental room (d).

not applicable to measure the surface of the windows, the internal surface temperature of windows was determined as a mean of 4 surface temperature measurements using T-type thermocouples. Thermocouples were shielded using aluminum foil and were taped to the surface of the inner pane of glass. The uncertainty of thermocouples was ± 0.2 °C, and the frequency of measurements was 3 s.

Parameters related to different dimensions of the thermal environment were measured every second on a vertical stand 0.2 m away from the person at 4 heights (0.1, 0.6, 1.1, 1.7 m). As shown in Fig. 3(c), the dry bulb temperature was measured with a PT100 sensor (± 0.15 °C), and air speed was measured with an omnidirectional hot sphere anemometer (Sensor Electronic, ± 0.02 m/s). Relative humidity was measured in the center of the room using a HOBO U12-012 (Onset, USA). The overall layout of environmental sensors in the room is illustrated in Fig. 3(d).

(b) Wearable sensing:

The local skin temperature and clothing temperature of a test subject were measured using iButton® temperature loggers DS1922L (MAXIM Integrated, USA). The accuracy of the sensors is ± 0.25 °C. Skin temperature was measured at 24 locations, and clothing temperature at 6 locations (right anterior thigh, right abdomen, left upper arm, left upper chest, right scapula, left posterior thigh). Skin temperature measurements at 14 locations (forehead, neck, right scapula, left upper chest, right arm in upper location, left arm in lower location, left hand, right abdomen, left paravertebral, right anterior thigh, left posterior thigh, right chin, left calf, right instep) were chosen according to ISO 9886:2004 14-point weighting scheme; additional 10 points (left and right fingertips, left arm in upper location, right arm in lower location, right paravertebral, left anterior thigh, right posterior thigh, left chin, right calf, left instep) were considered to better capture asymmetric

thermal exposure of the body. The sensors were attached to the skin and surface of clothing using medical permeable tapes. The frequency of all skin temperature measurements was 10 s.

2.2. Modeling

2.2.1. Radiant heat transfer model

The radiant heat transfer model in this study was constructed using a ray-tracing method in the Grasshopper/Rhino algorithmic 3D modeling software. This model accounts for the detailed geometry of the human body and its surrounding environment to better characterize the radiant energy exchanges between them. The radiation simulation contains two components, i.e., longwave radiation, which is emitted by the body and all the surrounding surfaces in its environment, and solar radiation, which is based on more conventional ray tracing simulations and is applied to the same human mesh model. The results of each portion can be derived separately and also combined to obtain MRT. This model can be used in two ways: firstly, to calculate the mean spherical irradiance from all directions falling onto a small sphere centered on the test point in space, showing the spatial variations of irradiance, or secondly, to calculate the BSPRT of all exposed body segments and show the BSPRT variations across the body.

(a) Longwave component

We use a vector-based ray-tracing technique in this study to simulate longwave radiation arriving at a body in space. Vectors spherically arrayed emanate from each test point on the body surface and represent directions of radiant heat flux. In order to account for multiple interreflections in the longwave portion, the heat flux vectors are traced through four bounces, and the radiant energy transmitted, emitted, or reflected can be obtained through their intersections with the surrounding surfaces. The detailed introduction of this method was explained in our previous paper [30,31], which illustrates the use of the ray-tracing simulation technique to calculate the longwave radiant temperature at the centroid of a segment of the body surface or the longwave radiant temperature of a point in space. If we assume that the BSPRT of a body segment (T_r) is the same for all points on the small segment and can be represented by the centroid of this segment; the calculation method for BSPRT will be identical to the radiant temperature at the centroid. For each ray-intersection, the surface temperature and the material properties (including reflectivity, emissivity, and transmissivity of the surface) are required for the calculation. Therefore, we embedded this information into the meshes of the geometry model. The reflectance coefficients of the main surfaces indoors are shown in Table 2.

The surface temperature data used for the mesh comes from three sources: the SMART sensor, infrared thermography, and thermocouples. The SMART sensor provides the majority of the data with the surface

Table 2
The reflectance and transmittance coefficients of the main surfaces indoors for receiving longwave and shortwave irradiation.

Surfaces	Longwave	Shortwave
<i>Reflectance</i>		
Floor	0.05	0.16*
Wall	0.10	0.70*
Ceiling	0.10	0.70*
Aluminum	0.90	0.90
LED Light	0.80	0.80
Furniture	0.10	0.30
<i>Transmittance</i>		
Double Glazing	0.30	0.36**

* Referenced from the technical specifications of the experimental facility, while others from [42].

** Measured in this study.

temperature readings of 4841 points in space during each experiment case (Fig. 5a). However, readings from SMART for the reflective surfaces in the room may not be accurate enough, so the readings from the eight thermocouples on the windows were used for creating the temperature meshes instead. After modeling all the exposed surfaces (including the walls, ceiling, floor, window, radiant panels, and furniture, etc.) and converting them into mesh with a grid size of around $0.1 \text{ m} \times 0.1 \text{ m}$ (or even smaller for narrow surfaces), the resulting meshes contain 12,837 faces and 15,039 vertices in total. With the coordinates of the measured points, the temperature readings from either SMART or thermocouples were assigned to the vertices of the mesh closest to the measured points (Fig. 5b). The temperature values of the remaining vertices of the mesh were assigned based on the least square interpolation method. The temperature of the locations without measured points nearby have been compared to the readings from the thermal images and therefore validated. As Fig. 6 shows, the surface temperature is represented by the color of the meshes of all surfaces indoors.

The human mesh model of the sitting subject was created using 3D scanning. The mesh initially contained 12,009 triangulated faces but was simplified to 3,916 meshes to save computational time while keeping the accurate shape. The surface temperature of the human mesh was assigned based on the readings from the iButton sensors. As shown in Fig. 7, we selected the readings of the sensors on the clothes (right scapula, left upper chest, right abdomen, right anterior thigh), or on the skin (forehead, neck, left arm in upper location, left arm in lower location, right arm in lower location, left hand, left fingertip, right fingertip) but uncovered by the clothes together to represent the surface temperature of the body exposed to the surrounding environment. In the following description, body temperature refers to the outermost surface temperature of the human body, whether it's for clothes or skin. In order to show the impact of body temperature as inputs for the simulation, another set of simulations without body temperature but only accounting for the rays not obstructed by the body have been prepared for the comparison (blue rays in Fig. 7b).

By checking for the rays emanating from every body segment but shaded by the body itself from the surrounding environment, the ray-tracing method can account for the effective radiation area of the body, which is defined as the surface area of the human body directly involved in radiation transfer with the environment. Previous studies provide effective radiation areas of the human body in common positions based on empirical experiments, and this was further used to calculate MRT and thermal comfort [12,13,43]. By separating rays obstructed by the body or not, MRT can be calculated with different input variables. Firstly, simply removing the rays obstructed by the body is suitable for calculating the whole-body MRT without body temperature as input (denoted as $MRT_{body-no}$). Another situation is to retain these rays and feed body temperature for calculating the whole-body MRT (denoted as MRT_{body}).

Besides calculating longwave BSPRT, the longwave mean spherical irradiance of points across the room was also calculated. Two testing planes were chosen: the first one is the plan in the horizontal direction which is 1.1 m above the floor, and the second one is the section in the vertical direction which is parallel to the East wall and is 1 m away from it. The planes are subdivided at the resolution of 0.1 m into small planes where the centroids become testing points for calculating mean spherical irradiance across the room. The horizontal and vertical planes have 1,860 and 1,922 testing points, respectively. The longwave portion of BSPRT ($T_{r,lw}$) of all body segments exposed to the surrounding environment or the longwave mean spherical irradiance of a point within a space (E_{lw}) can be derived.

(b) Solar radiation component

For the solar irradiance calculation, Honeybee (version 0.0.66), an environmental plugin in the Grasshopper/Rhino platform, was used.

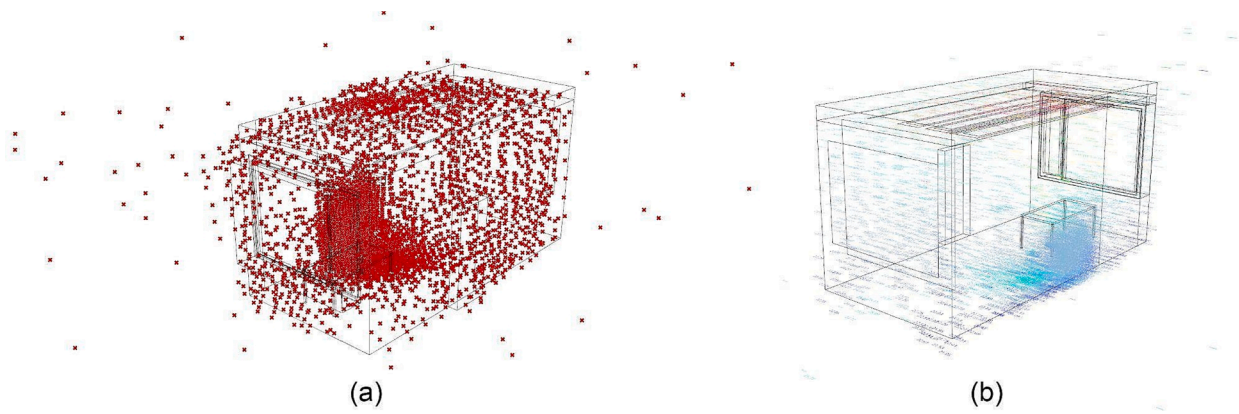


Fig. 5. Visualization of SMART scanning results: (a) Measured points, (b) Surface temperature of the measured points of SMART.

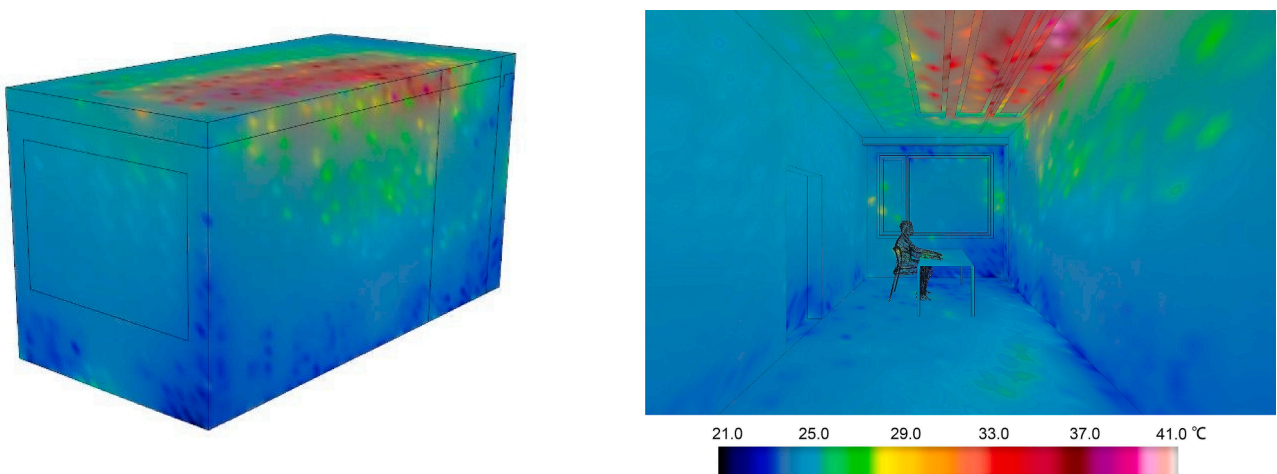


Fig. 6. Experimental room surfaces with the temperature mesh from the surface temperature data of SMART.

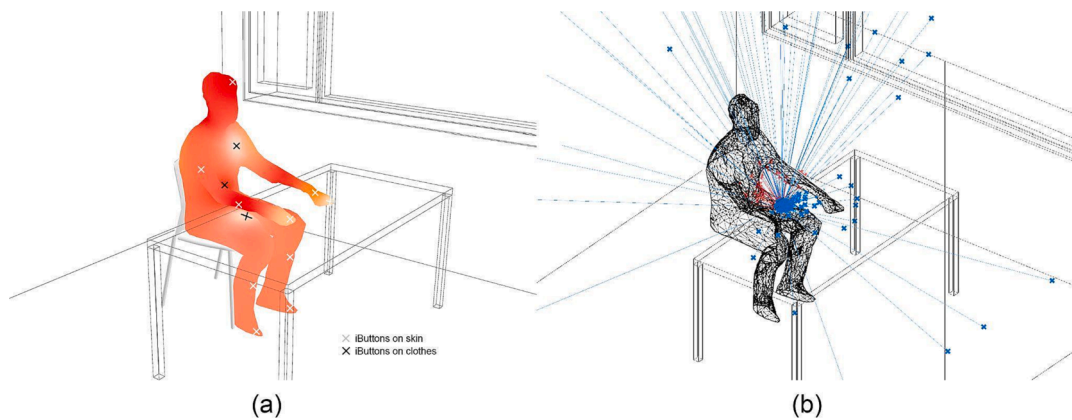


Fig. 7. (a) Human temperature mesh based on iButtons data; (b) Vectors emanating from the centroid of a plane surface for calculating BSPRT, with red rays obstructed by the body and blue rays not obstructed by the body.

With the given location (Fribourg, Switzerland, 46.8° latitude, 7.1° longitude) and the dates and times of the experimental cases, the sun path and the sun location for each case were determined. Since the minimum resolution of the time to build the sky model is one hour, the time to determine the sun location for each case is on the hour. For instance, the radiation simulation for Experiment I-a (10:17–10:47) used the sun location at 10:00; the simulation for Experiment II-b (13:47–14:17) was conducted twice for two periods, with the Sun location at 13:00 first and 14:00 s. The direct normal radiation and

diffuse horizontal radiation were measured using the SPN1 pyranometer. The averaged radiation during each period of the experimental cases was used as input for the sky model. The shortwave irradiance calculated for each test point or plane is based on the average for the duration of each period. In order to validate the shortwave radiation simulation component of Honeybee tools in this study, we placed lux meters at seven locations indoors during each experimental case and conducted the radiation simulation for the points at the same location as the sensors. The measured readings were used to compare with the

simulation results, and the difference between them is within the acceptable level ($\pm 10\%$) of the lux reading at that point in the room, providing a good estimation of the shortwave radiation arriving into the room.

Similar to the longwave component, the calculation methods for shortwave irradiance of a point or a plane are not identical. Firstly, in order to evaluate the shortwave irradiance received at a point from all directions in space, we adapted the simulation technique to calculate shortwave mean spherical irradiance (E_{sw}) as described in our previous paper [44]. The sample points for the shortwave radiation maps indoors are the same as those for the longwave MRT gradient maps, ensuring it can, later on, be added to the longwave component. Secondly, the shortwave portion of BSPT ($T_{r,sw}$) of all exposed body segments were calculated using the plane irradiance component from the RADIANCE engine [45]. The shortwave component simulation recipe was adapted to account for four bounces of the interreflections between reflective surfaces. The reflectance coefficients of materials of exposed indoor surfaces used for the shortwave radiation simulation is shown in Table 2.

In order to combine the simulated results of both shortwave and longwave components, BSPT needs to be converted to W/m^2 . The BSPT T_r (in $^{\circ}C$) of a body segment is calculated as follows:

$$E_r = \sigma \times (T_{r,sw} + 273.15)^4 + \sigma \times (T_{r,lw} + 273.15)^4 \quad (1)$$

$$T_r = \sqrt[4]{\frac{E_r}{\sigma}} - 273.15 \quad (2)$$

where E_r is the total radiated power of a body segment in W/m^2 , and σ is the Stefan-Boltzman constant as $5.67 \times 10^{-8} W/m^2K^4$. For all body segments exposed to the surrounding environment, the BSPT T_r will be calculated, and thus the MRT of the whole body MRT_{body} (in $^{\circ}C$) containing n body segments is:

$$MRT_{body} = \sqrt[4]{\frac{\sum_{i=1}^n A_i \times (T_{r,i} + 273.15)^4}{A}} - 273.15 \quad (3)$$

where the BSPT of the i^{th} body segment $T_{r,i}$ was weighted with the area of the body segment A_i , and A is the total body surface area. Moreover, the shortwave and the longwave portion of the whole body MRT, denoted as $MRT_{body,sw}$ and $MRT_{body,lw}$, can be calculated by substituting $T_{r,i}$ with the shortwave BSPT $T_{r,sw,i}$ and longwave BSPT $T_{r,lw,i}$ in Eq. (3) respectively. For further comparative study, the BSPT and MRT without body temperature as inputs were also calculated to evaluate the impact of body temperature on the final MRT.

Similarly, the mean spherical irradiance E_{point} of a point can be

$$MRT_{plane} = \frac{0.18 \times (t_{p-up} + t_{p-down}) + 0.22 \times (t_{p-left} + t_{p-right}) + 0.30 \times (t_{p-front} + t_{p-back})}{2 \times (0.18 + 0.22 + 0.30)} \quad (7)$$

calculated by summing the shortwave and longwave portions, and the MRT of a point within a space MRT_{point} (in $^{\circ}C$) is calculated as follows:

$$MRT_{point} = \sqrt[4]{\frac{(E_{point,sw} + E_{point,lw})}{\sigma}} - 273.15 \quad (4)$$

2.2.2. Overall thermal comfort

The overall thermal comfort index PMV was used in this study to characterize the thermal environment within the mechanically conditioned experimental facility. Four environmental parameters (air temperature, mean radiant temperature, air speed, relative humidity) and two personal parameters (metabolic rate, clothing insulation) were basic inputs for the thermal comfort model. PMV applies a 7-point ASHRAE

thermal sensation scale to evaluate thermal comfort or discomfort: neutral (0), slightly warm/cool (± 1), warm/cool (± 2), hot/cold (± 3). The calculated PMV index beyond the $-3 \sim +3$ range refers to extreme hot or cold situations.

Dry bulb temperature and air speed were measured by temperature sensors and anemometers of different heights attached to the stand near the subject (see section 2.1.2) for every second, and relative humidity was measured in the middle of the room for every ten seconds. These parameters were averaged during each experimental case. MRT was also calculated for each experimental case. The personal parameters remain unchanged during all experimental cases (metabolic rate 1.1 met, clothing insulation 0.57 clo). The inputs of the parameters for the PMV model are listed in Table 3.

With the inputs of the parameters described above, a Python package *pythermalcomfort* [46] was used to calculate PMV.

Two common calculation methods for MRT, the three-point method and plane method [47], were also used to compare with the full-body method developed in this study. The three-points method refers to weighting MRT from the mean radiant temperatures of three sample points representative of different parts of the body. For a sitting person, the points at the level of the ankle, the abdomen, and the head were at the heights of 0.1 m, 0.6 m and 1.1 m, respectively. The mean radiant temperatures of the three points in space (denoted as MRT_{point1} , MRT_{point2} , MRT_{point3} from low to high levels) were simulated using the ray-tracing method adopted in this study. The MRT from the three points (denoted as $MRT_{3points}$) is calculated by applying the weighting coefficients as Eq. (5) shows:

$$MRT_{3points} = \frac{1 \times MRT_{point1} + 2 \times MRT_{point2} + 1 \times MRT_{point3}}{4} \quad (5)$$

The plane method means calculating MRT from the plane radiant temperature (t_p) in six directions (denoted as t_{p-up} , t_{p-down} , t_{p-left} , $t_{p-right}$, $t_{p-front}$, t_{p-back}) and the projected area factors for a person in the same six directions. The plane radiant temperature in Celsius was calculated from the 6-directional shortwave K_i and longwave heat fluxes L_i with the absorption coefficients as Equation (6) shows:

$$t_{p,i} = \sqrt[4]{\frac{a_k K_i + a_l L_i}{a_i \times \sigma}} - 273.15K \quad (6)$$

where $a_k = 0.70$ and $a_l = 0.97$ are the absorption coefficients for shortwave and longwave radiant flux densities, σ is the Stefan-Boltzmann constant. When the orientation of the person is fixed, the MRT from plane radiant temperature (denoted as MRT_{plane}) can be calculated with the projection factors of a sitting person as:

The MRT was calculated using different methods (MRT_{point} accounting for a point at the location of the human body in space, and MRT_{body} , $MRT_{3points}$, MRT_{plane} accounting for the human body simplified to different degrees) was the input for calculating respective PMV. The PMV index can reveal the variations of different MRT calculation methods when characterizing the indoor thermal environment.

2.2.3. Radiant asymmetry

Radiant temperature asymmetry is commonly used to evaluate the local thermal discomfort in a radiant heterogeneous environment. The radiant temperature asymmetry is the difference between the plane

Table 3
The inputs of the parameters for the PMV thermal comfort model.

Parameter	Exp I			Exp II			Exp III		
	a	b	c	a	b	c	a	b	c
Air temperature, at 0.6 m (°C)	23.4	24.0	28.2	25.1	26.0	24.7	24.7	24.5	24.4
Air speed (m/s), at 0.6 m	0.05	0.05	0.10	0.10	0.10	0.07	0.04	0.05	0.05
Air temperature, at 1.1 m (°C)	24.4	25.0	28.4	26.7	27.8	26.3	25.1	24.9	24.7
Air speed (m/s), at 1.1 m	0.06	0.07	0.12	0.13	0.14	0.10	0.06	0.05	0.03
Relative humidity (%)	25.1	24.6	23.8	20.4	21.9	21.2	22.6	23.5	23.8

radiant temperature of the two opposite sides of a small plane element, which can be converted to irradiance in the unit of W/m². The position of the plane element should be referenced to the location of the studied subject, and the direction of the normal to the plane commonly corresponds to the left and right parts or the head and feet of the body.

Local body parts can have different sensitivities to cooling or warming [48]. This means the same radiant temperature asymmetry in different directions can result in local comfort or discomfort of varying degrees. The percentage dissatisfied (PD) is an index that can describe local discomfort, which means the thermal dissatisfaction caused by unwanted cooling or heating of one particular part of the body. According to ISO 7730 [47], radiant asymmetry can cause local discomfort when surfaces radiating at largely varying temperatures are involved (e. g., large glazing, thermally activated panels, etc.). Vertical radiant asymmetry can be caused by a warm ceiling or a cool ceiling, and horizontal radiant asymmetry can be caused by a warm wall or a cool wall, assuming left/right asymmetry caused the highest asymmetry discomfort compared to other positions, such as front/back asymmetry. For each situation, PD (in %) can be calculated with radiant temperature asymmetry (Δt_{pr} in °C) using Eqs. (8)–(11) [47].

$$PD_{warmceiling} = \frac{100}{1 + \exp(2.84 - 0.174 \cdot \Delta t_{pr})} - 5.5 \text{ for } \Delta t_{pr} < 23^\circ \text{C} \quad (8)$$

$$PD_{coolceiling} = \frac{100}{1 + \exp(9.93 - 0.50 \cdot \Delta t_{pr})} \text{ for } \Delta t_{pr} < 15^\circ \text{C} \quad (9)$$

$$PD_{warmwall} = \frac{100}{1 + \exp(3.72 - 0.052 \cdot \Delta t_{pr})} - 3.5 \text{ for } \Delta t_{pr} < 35^\circ \text{C} \quad (10)$$

$$PD_{coolwall} = \frac{100}{1 + \exp(6.61 - 0.345 \cdot \Delta t_{pr})} - 3.5 \text{ for } \Delta t_{pr} < 15^\circ \text{C} \quad (11)$$

2.2.4. Local thermal sensation and comfort

Thermal comfort and discomfort based on the local sensation of different body parts have been an important development in thermal comfort studies over the past decade. The human thermo-physiology model (HTPM) can be a handy tool to predict local skin and core temperatures. The results can then be used to project the local and overall thermal sensation and comfort of humans. When local environmental parameters are incorporated into the thermo-physiology model, the degree of modeling information improves. One of the important input parameters is the local mean radiant temperature and taking the radiant asymmetric factor into account increases the detail level of modeling.

We have adopted the open source human thermo-physiology model JOS3 [49]. The model includes 17 body parts, including the head, neck, chest, back, pelvis, right and left shoulders, arms, hands, thighs, legs, and feet. Furthermore, the results predicted are highly dependent on the subject’s posture, the position of the person inside the spaces, as well as other individual physiological factors, which are variable among individuals. The model takes into consideration individual factors, such as the age, gender, height, weight, and body fat. By evaluating the local ($T_{skin,i}$) and mean skin temperature ($T_{skin,mean}$) output from the HTPM, the local and overall thermal sensation of a person can be found based on, for instance, the model developed by Zhang et al. [50]. The model is capable of predicting local and overall thermal sensations for transient

and non-uniform environments. Based on Zhang’s model, the local sensation can be estimated as a function of local skin, mean skin, and core temperature.

3. Results

The experimental results will be presented in five parts: (3.1) solar irradiance, (3.2) longwave irradiance, (3.3) shortwave and longwave combined irradiance, (3.4) thermal comfort model, and (3.5) local thermal sensation, in order to analyze the influence of different thermal sources separately. For shortwave, longwave, and the combined portions, firstly MRT of points in the space ($MRT_{point,sw}$, $MRT_{point,lw}$ and MRT_{point}) is used to show the spatial variations in horizontal and vertical planes with testing points across the room. After that, the local thermal environment centered on the occupant is described by BSPRT ($T_{r,sw}$, $T_{r,lw}$ and T_r) variations across the body and the resulting MRT of the whole body ($MRT_{body,sw}$, $MRT_{body,lw}$ and MRT_{body}). In this study, we refer to “longwave mean radiant temperature (MRT_{LW})” and “shortwave mean radiant temperature (MRT_{SW})”, and the sum of longwave and shortwave components equals the final MRT for implementation within a thermal comfort model. Since there was no occupancy for Exp I-c, II-c, and III-c, so only MRT_{point} results are provided instead of BSPRT T_r and the MRT of the whole body MRT_{body} for these cases. In section 3.4, there are two comparative studies. At first, the MRT calculation method developed in this study that can model the irradiation on a full geometric model of the body is compared with the three-points method and plane method described in ISO 7726 [51], using $MRT_{body-no}$, $MRT_{3points}$, MRT_{plane} and their corresponding PMV. Moreover, including the measured body temperature in our MRT calculation method will make this model account for the local irradiance from other body segments, resulting in MRT_{body} , compared to $MRT_{body-no}$ without body temperature as inputs. When results are shown in Watts, it is the direct conversion of thermal emission to heat flux which is not dependent on emissivity. Emissivity be invoked when determining radiant heat exchange within the thermal comfort model. Finally, in section 3.5, the calculated weighted 17 local MRT for each body segment was used as non-uniform environmental input in a detailed human thermo-physiology model. The local thermal sensation was then calculated to highlight the differences in thermal sensation between the different body segments when a person is exposed to a radiantly heterogeneous environment.

The longwave MRT simulation was validated with the use of 6-directional pyrgeometers. The result for the point simulation located where the two pyrgeometers array were taken provided the average of longwave MRT of 25.5 °C and 25.3 °C, respectively, which are in good agreement with the readings of the pyrgeometers as 25.6 °C and 25.3 °C. The averaged variance percentage of the simulation results to pyrgeometer readings are 0.5 % and 0.3 % for the two points measured.

3.1. Solar irradiance

The range of shortwave Mean Radiant Heat Flux (MRX) of points $MRX_{point,sw}$ across the room, shortwave $BSPRX_{r,sw}$, portion of the whole-body MRX $MRX_{body,sw}$ and related indicators of all experimental cases are shown in Table 4. In experimental case I-a, the direct sunlight came from the Southeast direction, therefore, the subject did not receive the direct

Table 4
 $MRX_{point,sw}$ and $BSPRX_{r,sw}$ variations in all experiments.

Parameter		Exp I			Exp II			Exp III		
		a	b	c	a	b	c	a	b	c
$MRX_{point,sw}$ across the plane (W/m^2)*	Plan-horizontal	2.9– 85.0	3.0–79.9	3.1– 84.1	2.2–80.1	2.4–75.3	2.0–62.8	0.0–42.9	0.0–26.0	0.0–9.1
	Section-vertical	0.2–50.3	0.1–69.5	0.2–71.7	0.1– 75.1	0.1–73.2	0.2–61.8	0.0–43.3	0.0–26.2	0.0–9.1
$BSPRX_{r,sw}$ of the sitting subject's segments (W/m^2)**	$MRX_{body,sw}$	12.6	33.1	–	41.7	39.4	–	0.3	0.2	–
	Range	0.0–	0.1–	–	0.1–	0.0–	–	0.0–1.4	0.0–0.9	–
		152.1	192.2	–	216.8	199.3	–	–	–	–
	Standard deviation	18.6	50.4	–	62.5	56.1	–	0.2	0.2	–
	Asymmetry Left-Right	14.1	86.2	–	111.2	100.3	–	0.4	0.2	–
	Asymmetry Up-Down	8.2	40.6	–	65.1	59.3	–	0.1	0.1	–

* $MRX_{point,sw}$ in W/m^2 is equal to shortwave mean spherical irradiance $E_{point,sw}$.
 ** The subject sits on the chair next to the desk for the cases with occupancy.

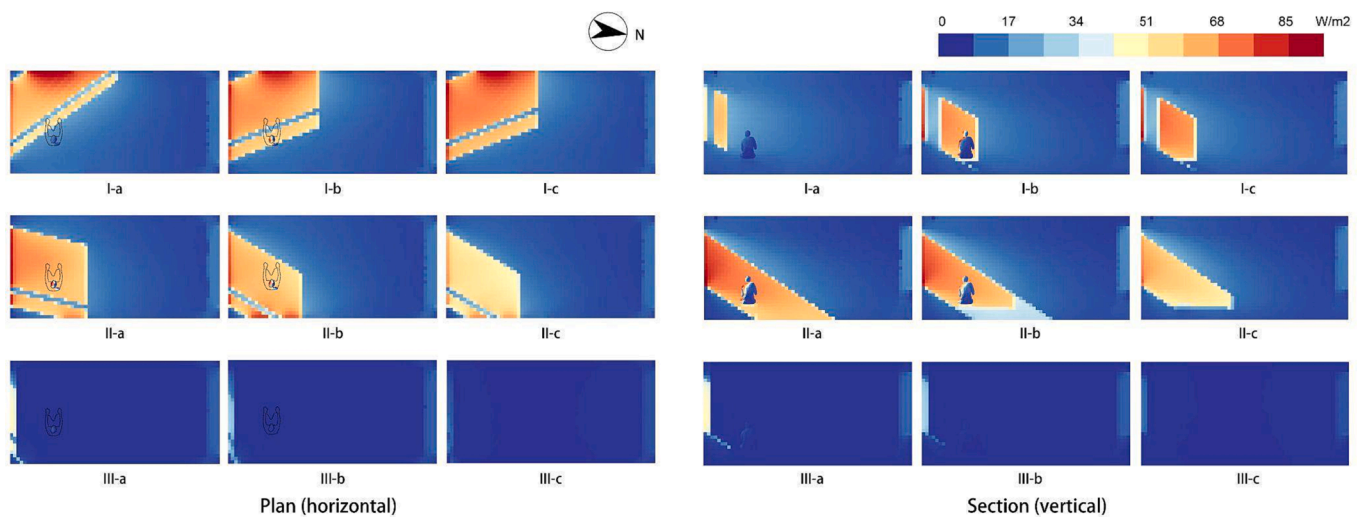


Fig. 8. Spatial variations of $MRX_{point,sw}$ (W/m^2) in the horizontal plane at the height of 1.1 m (left) and vertical section (right). The range of values for each case are listed in Table 4.

sunlight. As the sunlight's direction moved near South and the solar radiation increased, the overall $MRX_{point,sw}$ received indoors increased and reached the peak in Exp I-c at around 12 pm, as is shown in Fig. 8. In Exp II-a, the $MRX_{point,sw}$ at the location around the subject reached the peak when direct shortwave radiation was least obstructed by the building envelope. After that, both direct normal radiation and diffuse horizontal radiation decreased, so the $MRX_{point,sw}$ indoors has decreased, too. In Exp III (15:34–17:31) when the blinds of the South and North windows were all down, the $MRX_{point,sw}$ within the room was lower than $10 W/m^2$, except for the small gap area between the South window and

the blinds.

The overall shortwave irradiance in Exp I-a was not the highest, but the maximum $MRX_{point,sw}$ was the highest among all experimental cases as $85.0 W/m^2$, which was received at the location near the reflective aluminum sheet on the West wall (Fig. 4a). The aluminum sheet received most direct sun rays in this case and contributed to more reflected shortwave irradiation than later cases.

The $MRX_{body,sw}$, namely the average shortwave $BSPRX_{r,sw}$ of all exposed body segments weighted by surface area, had a large increase from Exp I-a to Exp I-b because of the direct sunlight. It kept increasing and peaked at $41.7 W/m^2$ in Exp II-a (Fig. 9). After the blinds of the

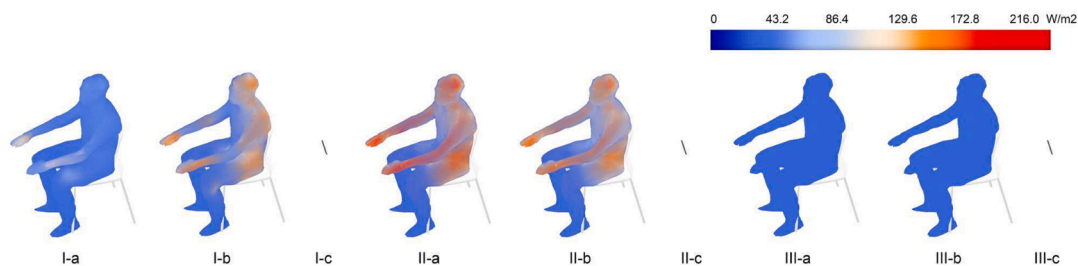


Fig. 9. Shortwave Body Segment Plane Radiant Temperature $BSPRX_{r,sw}$ variations (W/m^2) with the range and $MRX_{body,sw}$ of each case presented in Table 4. (Note: there was no occupancy in Exp I-c, II-c and III-c).

South window were down, the $MRX_{body,sw}$ decreased sharply to 0.3 W/m² in Exp III. Since the direct sunlight comes through the South window, the body surfaces facing the South window, especially the left side of the head, abdomen, and both arms, received more shortwave radiation than other parts. This results in the shortwave radiant asymmetry in the left–right direction and up–down direction. As the maximum $BSPRX_{r,sw}$ reached a peak of 216.8 W/m² in Exp II-a, the degree of asymmetry was also the highest in both directions, which means the shortwave irradiance falling on the left side was 111.2 W/m² higher than the right side, and that on the top was 65.1 W/m² higher than the underside (Table 4). In comparison, when the subject received only diffuse shortwave radiation in Exp I-a, the shortwave radiant asymmetry was much lower, with 14.1 W/m² in the left–right direction and 8.2 W/m² in the up–down direction. With both the least direct and diffuse shortwave irradiance indoor, the shortwave radiant asymmetry was reduced to nearly 0 W/m² in Exp III.

3.2. Longwave irradiance

The range of longwave MRX of points $MRX_{point,lw}$ across the room, longwave $BSPRX_{r,lw}$ portion of the whole-body $MRX_{body,lw}$, and related indicators of all experimental cases are shown in Table 5. In Exp I-a and I-b, the $MRX_{point,lw}$ varied largely across the room, forming two zones, one is the upper area near the radiant panels on the ceiling and the area around the South window, where the $MRX_{point,lw}$ is generally 17.9 W/m² (3 °C for $MRT_{point,lw}$) higher than the surrounding area (Fig. 10). The overall $MRX_{point,lw}$ within the space gradually increased and reached the peak (maximum 461.1 W/m²) in Exp II-b (13:47–14:17), which was approximately 2 h later than the peak of the shortwave portion $MRX_{point,sw}$. The $MRX_{point,lw}$ difference across the room gradually reduced as the northern portion of the room warmed up due to the longwave radiation reflected among room surfaces. In Exp III, the longwave irradiation field was uniform within the space with a difference of less than 9.9 W/m² (1.7 °C for $MRT_{point,lw}$), and $MRX_{point,lw}$ did not decline as sharply as $MRX_{point,sw}$ after the blinds of the South window were down.

The $MRT_{body,lw}$ of the body was 26.2 °C (455.4 W/m² for $MRX_{body,lw}$) in Exp I-a with an increasing trend, and the highest was 27.3 °C (462.1 W/m² for $MRX_{body,lw}$) in the same case as the $MRT_{point,lw}$, that is Exp II-b (Table 5). It gradually decreased to 26.6 °C (457.7 W/m² for $MRX_{body,lw}$) in Exp III, resulting in a small variation over all experimental cases. The longwave radiant asymmetry was not obvious overall, for the highest was 0.4 °C (2.7 W/m²) in the left–right direction and 1.2 °C (7.5 W/m²) in the up–down direction, and both situations happened in Exp II-b. The body parts having high $T_{r,lw}$ were the upper side of thighs, abdomen, neck, and inner side of arms, which were mostly self-occluded and therefore influenced by the body itself. The subject received more

longwave heat fluxes from the right than the left in Exp I-a, III-a and III-b, when the solar radiation impact was negligible. Also, the longwave radiant asymmetry in the up–down direction was high in these cases, due to the longwave radiation from the radiant panels and the warmed up room surfaces.

The simulation results of longwave BSPRT without body temperature as inputs $T_{r,lw-no}$ have a small range (24.4–27.7 °C), which is almost 4.5 °C lower than the $T_{r,lw}$ in the original testing set (Table 6). High $T_{r,lw-no}$ appears around the head, shoulder, arms, and thighs, but $T_{r,lw-no}$ in all cases is lower than the body temperature since the surface temperature of the surrounding environment is basically lower than the body temperature. The resulting MRT of the whole body (without body temperature as input) $MRT_{body,lw-no}$ in all cases is around 1 °C lower than $MRT_{body,lw}$ in the original set.

3.3. Shortwave and longwave combined irradiance

The range of shortwave and longwave combined MRX of points across the room MRX_{point} , $BSPRX$, whole-body MRX_{body} and related indicators of all experimental cases are shown in Table 7. The spatial MRT_{point} variations had a similar pattern and trends in plan and section view (Fig. 11) as the shortwave portion $MRX_{point,sw}$. The overall MRX_{point} increased from the morning and reached a peak of 540.1 W/m² (39.3 °C for MRT_{point}) at around 12 pm, then decreased slowly in Exp II and sharply in Exp III. The MRT_{point} at the same location of the subject reached the peak in Exp II-b when the MRT_{body} of the sitting subject also reached the peak as 33.5 °C (Table 8). Without direct sun rays in Exp I-a, the MRT_{body} was much lower as 28.3 °C and it decreased to 26.6 °C when there was no solar radiation coming indoors in Exp III.

The subject sitting by the desk did not receive much direct sunlight in Experiment I-a, and the radiant asymmetry was 2.2 °C (14.1 W/m²) in the left–right direction and 2.4 °C (14.6 W/m²) in the up–down direction. Since Experiment I-b, the subject was in a highly irradiated area within the space mainly because of direct sun rays. The left side of the head, neck, arms and abdomen received higher irradiance than other parts, resulting in the highest radiant asymmetry as 16.4 °C (113.3 W/m²) in the left–right direction and 11.2 °C (71.7 W/m²) in the up–down direction, which could result in the highest PD as 23.4 % in the vertical direction but lower PD in the left–right direction. When the thermal sensation of the subject is warmer than neutral, the local discomfort of the subject caused by side-to-side radiant asymmetry is less sensitive than that caused by vertical asymmetry.

Responses of the subject confirm thermal discomfort experienced during experimental cases II-a and II-b. The subject was feeling “slightly uncomfortable”, “slightly warm”, and preferred to be colder. He was feeling warm in certain body parts on the left; particularly, his head,

Table 5
 $MRX_{point,lw}$ and $BSPRX_{r,lw}$ variations in all experiments.

Parameter		Exp I			Exp II			Exp III		
		a	b	c	a	b	c	a	b	c
$MRX_{point,lw}$ across the plane (W/m ²)*	Plan-horizontal	440.0-	441.4–459.3	443.9-	443.7-	445.4-	445.8-	445.3-	445.5-	444.7-
		456.3		459.3	457.7	460.7	458.1	455.2	453.7	452.9
	Section-vertical	439.7-	441.2-	445.2-	444.4-	447.2-	447.2-	447.0-	447.1-	446.2-
		453.1	456.9	458.9	458.0	461.1	459.5	455.5	455.1	454.9
$BSPRX_{r,lw}$ of the sitting subject’s segments (W/m ²)**	$MRX_{body,lw}$	455.4	457.6	–	459.2	462.1	–	458.2	457.7	–
	Range	445.8-	446.1-	–	449.8-	450.8-	–	450.2-	449.9-	–
		481.1	484.4		485.9	493.1		484.2	484.6	
	Standard Deviation	6.9	7.1	–	7.2	8.2	–	6.3	6.2	–
	Asymmetry Left-Right	–0.1	1.0	–	2.1	2.7	–	–0.4	–1.1	–
	Asymmetry Up-Down	6.4	5.6	–	6.6	7.5	–	5.2	3.9	–

* $MRX_{point,lw}$ in W/m² is equal to longwave mean spherical irradiance $E_{point,lw}$.

** The subject sits on the chair next to the desk for the cases with occupancy.

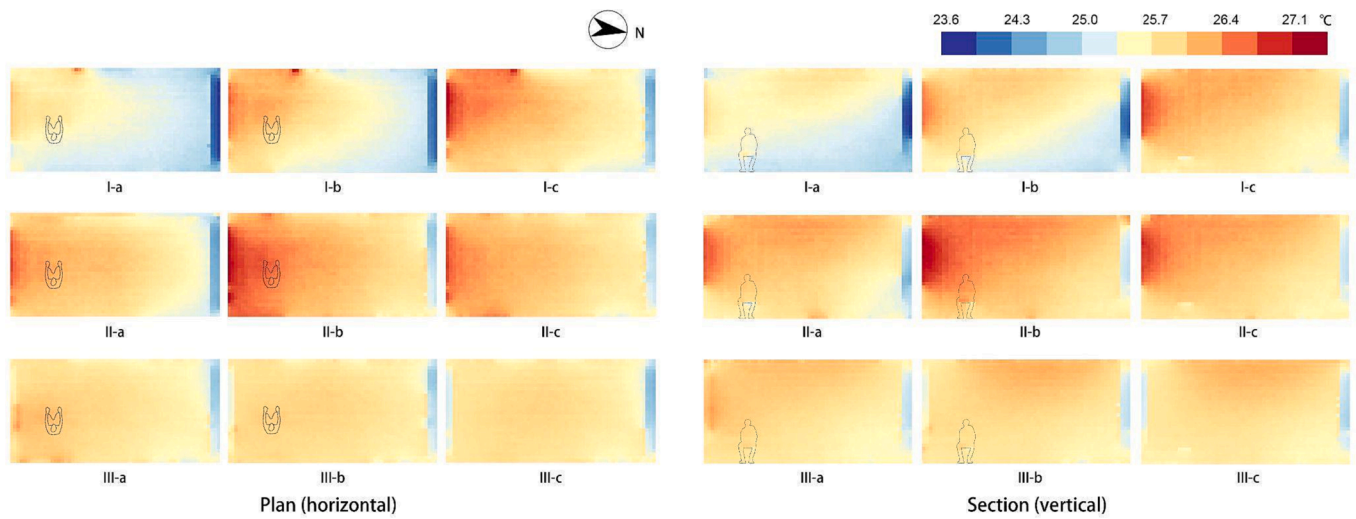


Fig. 10. Spatial variations of $MRT_{point,lw}$ (°C) in the horizontal plane at the height of 1.1 m (left) and vertical section (right). The range of values for each case are presented in Table 5.

Table 6

Longwave body segment plane radiant temperature $T_{r,lw}$ (with body temperature as inputs) and $T_{r,lw-no}$ (without body temperature as inputs) variations.

(°C)									
Exp.	I-a	I-b	I-c	II-a	II-b	II-c	III-a	III-b	III-c
With body temperature as inputs									
			-			-			-
$MRT_{body,lw}$	26.2	26.6	-	26.8	27.3	-	26.7	26.6	-
$T_{r,lw}$	24.6-30.4	24.7-30.9	-	25.3-31.1	25.5-32.2	-	25.4-30.8	25.3-30.9	-
Without body temperature as inputs									
			-			-			-
$MRT_{body,lw-no}$	25.2	25.6	-	25.8	26.2	-	25.8	25.7	-
$T_{r,lw-no}$	24.4-26.7	24.4-27.1	-	24.4-27.3	24.4-27.7	-	24.5-27.0	24.4-26.8	-

chest, back, upper arm, forearm, and hand on the left side were warm. No strong overall and local thermal discomfort was experienced during the rest of experimental cases.

Similar to the results of the longwave component, the MRT of the whole body (without body temperature as input) $MRT_{body-no}$ in all cases is around 1 °C lower than the MRT_{body} in the original test (Table 8). The maximum BSPRT T_{r-no} did not lower as much as the longwave portion $T_{r,lw-no}$ because of the large contribution from the shortwave component, for which the body temperature is not needed for the simulation. In conclusion, it is proved that neglecting the radiant heat fluxes from the body itself can result in a large MRT variation.

3.4. Thermal comfort model

Parameters MRT_{point} across the room, MRT_{point} of the point at the location of the subject, MRT_{body} and their corresponding PMV of all experimental cases is shown in Table 9. When the overall spatial MRT_{point} of points at the height of 1.1 m reached the peak in Exp I-c with the maximum as 39.3 °C, the most uncomfortable situation with the PMV from point-based MRT (denoted as PMV_{point}) of 2.45, which means the sensation between warm and hot, appeared in the area near the reflective aluminum sheet on the West wall and near the window. According to the PMV_{point} at the location of the subject sitting by the table, the warmest situation was in Exp I-c when the direct sunlight came from the South, and only experimental cases during which the subject did not receive direct sunlight were within the $-0.5 \sim +0.5$ comfortable range

Table 7
 MRX_{point} and $BSPRX$ variations in all experiments.

		Exp I			Exp II			Exp III		
		a	b	c	a	b	c	a	b	c
MRX_{point} across the plane (W/m^2)*	Plan-horizontal	447.1–536.0	447.7–534.5	450.3– 540.1	448.8–537.7	450.3–537.3	449.5–520.2	447.7–495.8	448.1–476.2	447.6–457.8
	Section-vertical	446.5–501.5	447.3–524.5	449.3–528.9	449.1–531.9	450.9– 532.7	450.5–519.3	448.8–497.1	449.0–476.4	448.5–457.6
$BSPRX$ of the sitting subject's segments (W/m^2)**	MRX_{body} Range	468.0	490.7	–	501.0	501.5	–	458.5	457.9	–
	Standard Deviation	447.1–612.6	447.9–655.5	–	451.0– 686.3	452.2–674.0	–	450.2–484.2	449.9–484.6	–
	Asymmetry Left-Right	20.2	51.3	–	64.2	58.4	–	6.2	6.2	–
	Asymmetry Up-Down	14.1	87.2	–	113.3	103.0	–	0.0	–0.6	–
		14.6	46.1	–	71.7	66.8	–	5.3	4.0	–

* MRX_{point} in W/m^2 is mean spherical irradiance E_{point} .

** The subject sits on the chair next to the desk for the cases with occupancy.

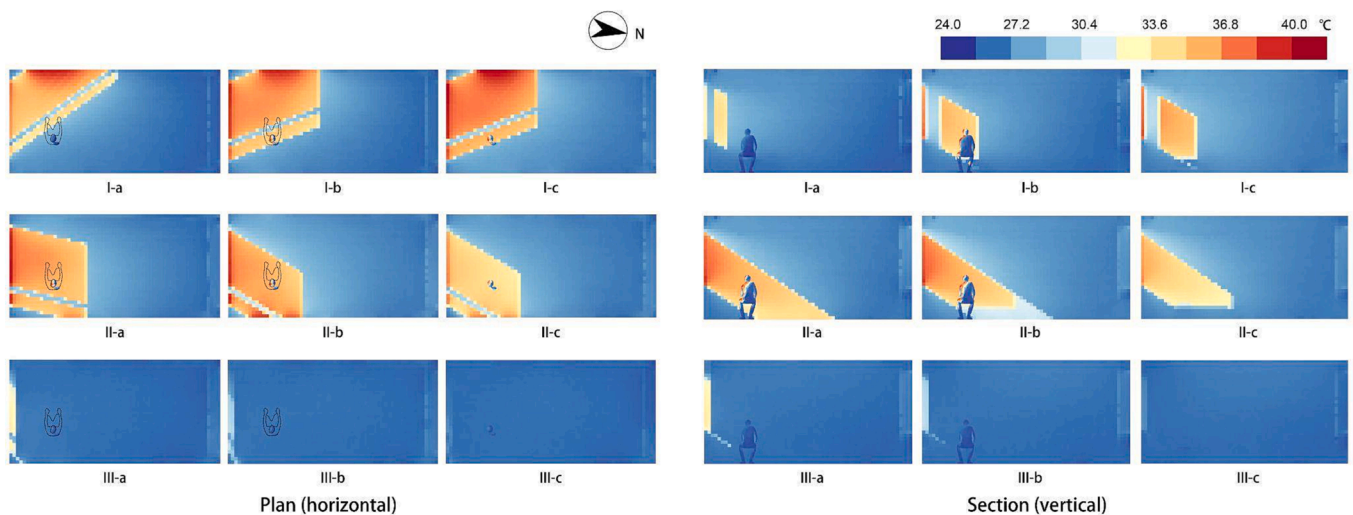


Fig. 11. Spatial variations of MRT_{point} (oC) in the horizontal plane at the height of 1.1 m (left) and vertical section (right). The range of values for each case is presented in Table 7.

(Exp I-a, and III-a, b, c). The whole-body MRT (with the body temperature as input) MRT_{body} was also high for the cases with direct sunlight, resulting in the maximum PMV from whole-body MRT (denoted as PMV_{body}) of 1.27 in Exp II-b, which means slightly warm (when Exp I-c, II-c, and III-c without occupancy did not provide body temperature for the calculation).

For comparing the MRT calculation method developed in this study that accounts for the whole-body geometry with other methods that simplify the body geometry to different degrees, the MRT calculated from the three-points method ($MRT_{3points}$), radiant plane temperature method (MRT_{plane}) were compared to the MRT accounting for the full body but without the body temperature as input (MRT_{bd-no}). It is to be noted that $MRT_{body-no}$ instead of MRT_{body} should be used for this comparison focusing on the geometry simplification since the three-point method and plane methods don't use the body temperature for the MRT calculation. In experimental cases with the least shortwave radiation (Exp III), the MRT from the three methods shows the most approximation with each other. The second least difference in MRT was for the cases during which the subject was in the area receiving shortwave radiation (Exp II), and this can be observed in the plan (Fig. 8). The $MRT_{3points}$ and MRT_{plane} were within a variation of around ± 0.5 °C

compared to $MRT_{body-no}$. When the subject was not completely in the area receiving shortwave radiation (Exp I), which means a more radiant heterogeneous environment around the subject, the variation enlarged to around ± 1 °C. This results in a PMV variation of around ± 0.2 .

The impact of the body temperature as input for the MRT calculation can be revealed by the difference between the MRT of the whole body with (MRT_{body}) or without ($MRT_{body-no}$) temperature input. $MRT_{body-no}$ is on average 1 °C lower than MRT_{body} , resulting in the PMV from $MRT_{body-no}$ (denoted as $PMV_{body-no}$) is around 0.2 lower than that from MRT_{body} (denoted as PMV_{body}). This shows the importance of body temperature for MRT calculation and, thus, comfort evaluation.

3.5. Local thermal sensation

To determine the local thermal sensation, the first two periods (a and b) of the three experimental scenarios when the subject was in the room were used. The simulation of HTPM was initialized by running it at a uniform environment of 25 °C operative temperature. Afterward, experimental inputs of the environmental parameters such as air speed, air temperature, and relative humidity were used. The measured body composition of the subject used in the simulation (height of 1.75 m, 72.9

Table 8
Body segment plane radiant temperature T_r (with body temperature as inputs) and T_{r-no} (without body temperature as inputs) variations.














										
Exp.	I-a	I-b	I-c	II-a	II-b	II-c	III-a	III-b	III-c	
With body temperature as inputs										
			-			-			-	
MRT_{body}	28.3	31.9	-	33.4	33.5	-	26.7	26.6	-	
T_r	24.8-49.3	25.0-54.8	-	25.5-58.5	25.7-57.0	-	25.4-30.8	25.3-30.9	-	
Without body temperature as inputs										
			-			-			-	
$MRT_{body-no}$	27.3	30.9	-	32.5	32.4	-	25.8	25.7	-	
T_{r-no}	24.5-48.3	24.4-53.9	-	24.4-57.3	24.4-55.5	-	24.5-27.1	24.4-26.8	-	

Table 9
 MRT_{point} , MRT_{body} ($MRT_{3points}$), plane (MRT_{plane}) and full body ($MRT_{body-no}$) and corresponding PMV variations in all experiments.


Parameter		Exp I			Exp II			Exp III		
		a	b	c	a	b	c	a	b	c
Spatial variation	$MRT_{point}(^{\circ}C)$	24.8-	24.9-	25.4-	25.1-	25.3-	25.2-	24.9-	25.0-	24.9-
		38.7	38.5	39.3	38.9	38.6	36.3	32.7	29.6	26.6
	PMV_{point}	-0.27-	-0.20-	0.31-	-0.06-	0.14-	0.01-	-0.16-	-0.16-	-0.20-
		1.84	1.90	2.45	1.99	2.13	1.76	1.01	0.52	0.04
Point at the location of the subject -0.6 m	$MRT_{point}(^{\circ}C)$	26.6	33.7	34.3	34.7	34.6	32.6	25.9	25.8	26.6
	PMV_{point}	-0.19	0.98	1.76	1.31	1.44	0.92	-0.08	-0.11	-0.19
Whole-body	$MRT_{body}(^{\circ}C)$	28.3	31.9	-	33.4	33.5	-	26.7	26.6	-
	PMV_{body}	0.05	0.70	-	1.11	1.27	-	0.04	0.01	-
3 points ($^{\circ}C$)	$MRT_{3point}(^{\circ}C)$	26.6	32.0	32.5	32.7	32.7	31.3	25.8	25.7	-
	PMV	-0.19	0.72	1.47	1.00	1.13	0.72	-0.09	-0.13	-
Plane	$MRT_{plane}(^{\circ}C)$	26.3	31.3	31.8	31.8	31.9	31.0	25.9	25.8	-
	PMV	-0.23	0.61	1.35	0.87	1.01	0.67	-0.08	-0.11	-
Full body	$MRT_{bd-no}(^{\circ}C)$	27.3	30.9	21.4	32.5	32.4	31.2	25.8	25.7	-
	PMV_{bd-no}	-0.09	0.55	1.27	0.97	1.09	0.71	-0.09	-0.13	-

kg of weight, 28.2 % of fat percentage, and 1.98 m² of body surface area). The radiant temperature of body segments BSPRT varied from 26.4 to 43.1 °C after averaging the data of small surface area within every one of the 17 segments. Table 11 shows the local mean radiant temperature of the 17 body parts that include both longwave and shortwave radiation. The areas exposed to direct sunlight from the left, e.g., the left side of the head, abdomen and both arms, had significantly higher radiant temperatures than other parts. By averaging the radiant temperature of all segments with the surface area of the segments as weighted coefficients, the whole-body MRT can be calculated. The human subject had the highest MRT above 33 °C in the second session

and the lowest in the third session, as is shown in Table 10.

The human thermo physiology model JOS3 was linked to the detailed local sensation model of Zhang (2010). The results from the model showed that during the first session, when MRT showed elevated values in the second half-hour of the session reached 31 °C, the overall sensation increased from neutral to warm with a value of 2 on the 9-point scale. In the second session, MRT was high during the whole period, and that was reflected in the overall sensation with a value of + 3, which corresponds to "hot". As for the third session, the solar radiation was almost negligible, with MRT values fluctuating around 1 °C higher than the air temperature, and the overall sensation was in the neutral range.

Table 10
Weighted body segment planar radiant temperature (BSPRT) variations during the experiments.









Exp.	I-a	I-b	I-c	II-a	II-b	II-c	III-a	III-b	III-c
			-			-			-
BSPRT	26.4-35.1	26.6-40.6	-	26.7-43.1	27.2-42.3	-	26.1-27.6	26.0-27.5	-

Table 11
Local thermal sensation and overall sensation prediction over the different experimental sessions using the 9-point sensation scale.

Cases	Head	Neck	Chest	Back	Pelvis	L Shoulder	R Shoulder	L Arm	R Arm	L Hand	R Hand	L Thigh	R Thigh	L Leg	R Leg	L Foot	R Foot	Overall	
Exp. I	a	0.9	1.4	0.3	-0.4	-0.1	0.0	-0.1	0.0	-0.6	-0.4	-0.2	-0.4	-0.7	-0.7	-1.3	-1.4	0.6	
	b	3.6	2.8	1.2	0.9	0.4	0.9	0.0	0.3	-0.1	0.9	0.7	-0.1	-0.4	-0.7	-0.8	-1.3	-1.3	1.9
Exp. II	a	2.6	2.5	1.1	0.1	-0.2	0.9	0.1	1.3	1.2	1.0	0.8	0.0	-0.3	-0.6	-0.6	-1.0	-1.0	1.8
	b	3.8	2.9	2.5	1.8	0.3	1.6	0.6	3.0	2.9	2.3	2.1	0.3	0.0	0.9	0.9	1.7	1.7	3.3
Exp. III	a	-0.2	1.1	0.0	-0.5	-0.2	-0.1	-0.1	-0.5	-0.6	-0.5	-0.5	-0.1	-0.1	-0.1	-0.1	-0.2	-0.2	0.4
	b	0.1	0.8	0.2	-0.3	0.1	-0.1	-0.1	-0.9	-0.9	-0.7	-0.7	-0.2	-0.2	-0.5	-0.4	-0.9	-0.9	-0.2

Noting the local sensation values presented in Table 11, the sensation of the head was the highest and the most sensitive body part toward the elevated temperature. The differences between the left and right can be seen in the shoulders, where sensation has higher values for the left shoulder, especially during exposure to solar radiation. The difference in sensation between the left and right shoulders was around one point on the 9-point scale, which shifted the shoulder from neutral to slightly warm.

4. Discussion

4.1. Spatial MRT variation across the room

The spatial MRT_{point} distribution through space varies significantly, as shown in the planar plots at 1.1 m height throughout the space. Whereas a very common method in experimentation is to use a globe to measure one, or at best, four points in space, we were able to provide a full mapping of the radiant field. Moreover, we were able to account for both longwave and shortwave variations throughout the space with accurate room geometries. The experimental setup of an office space with a window shows that MRT can vary significantly throughout the room. The range of longwave MRT $MRT_{point,lw}$ simulated for points throughout the room was 23.6–27.1 °C (439.7–461.1 W/m² for $MRX_{point,lw}$). Shortwave MRX of points $MRX_{point,sw}$ varied between 0–85.0 W/m². The combined shortwave and longwave MRT MRT_{point} variations were 24.8–39.3 °C (446.5–540.1 W/m² for MRX_{point}). The variation of MRT found in our analysis is of a similar range of the shortwave and longwave results described by Lee for a room with solar gains moving through the space from a window [26]. The longwave variations were also similar to our previous work [29], but neither are for the same space or control so cannot be directly compared but demonstrate the methods appear reasonable. Compared to work on outdoor shortwave [25,28], the variation in shortwave load can be much

higher outdoors.

According to the PMV model, these variations would result in comfort outputs that vary from -0.27 to 2.45 as compared to the singular value that would be reported for a room with one globe at 1.1 m. In comparison, the recommended range of PMV for comfort is from -0.5 to 0.5, and the PMV of an office room can range from -0.4 to 0.6 with an air-conditioner [52] or from -0.6 to -0.2 [53], which is much narrower than the PMV range in this study. While these variations are largely influenced by solar exposure in our case study, which may or may not be present in other scenarios, we believe that our methods have the potential to uncover variations that previous more averaged methods do not.

4.2. Comparing body MRT calculation methods

We compared three different methods of calculating a body-weighted MRT: the average of simulated MRT at three different heights - 0.1 m, 0.6 m, and 1.1 m ($MRT_{3points}$), the weighted plane radiant temperature inputs from horizontal and vertical directions (MRT_{plane}), and the method we developed to find the weighted average of the radiant temperature for all segments of a human body mesh ($MRT_{body-no}$). Using our method, we were able to model the irradiation on a full geometric model of the body and get an average $MRT_{body-no}$ of a person in any position. Furthermore, we used the data from the iButtons placed on the subject to apply local surface temperature values to the body, which in turn impacts the MRT since the body shades itself from the environment and temperature variations of skin and cloths contribute to the radiant temperature range perceived by the body (resulting in a final MRT denoted as MRT_{body}). While Fanger and others have addressed this issue with the generalization of varied view factors in the effective radiation area factor, we are able in our method to accurately simulate the impact of self-shading resolved across different body positions and clothing or skin temperatures.

4.3. Implications of MRT variation

The $MRT_{body-no}$ is the closest to the MRT as defined by ASHRAE and others, where MRT should be the equivalent temperature to what is experienced by a human body – implying that the full human body geometry should be accounted for. While ISO 7726 recognizes that heterogeneous radiation can result in variations across the body and recommends using the 3-points of measurement at different heights to calculate MRT ($MRT_{3points}$, as indicated by Equation (5), still, the “mean” aspect of the MRT framework fails to address the variation we have illustrated across the body of both shortwave and longwave components in multiple directions. In other words, $MRT_{3points}$ or even MRT_{body} alone cannot fully represent the impact of radiant heat on comfort in a heterogeneous environment. This has been partially addressed by considering the radiant asymmetry in previous work [22] where MRT might be a more thermally neutral temperature, but significant differences between surfaces may exist. Still, radiant asymmetry only considers directly opposing surfaces, and this may overlook more significant variations in thermal load on different parts of the body that may not necessarily be represented by opposing planes. The range of BSPRT (T_r) across the body shown in Table 8 demonstrates a very significant variation. For example, in Experiment II-a the hottest body segment was 58.5 °C (located at the left side of the subject’s neck), and the coldest segment was 25.5 °C (located at the left side of the subject’s left knee).

Many past researches have identified methods to consider different body parts’ influence within the MRT model using abstractions of the body or a manikin, but here we present a live high-fidelity thermal-scan of the occupant as an input for the ray tracing process. The scans demonstrate large heterogeneity in terms of perceived radiant temperature across the human body that can directly be used without simplifying the geometry of either the space or the human body. It is not decided whether one would have increased or decreased thermal comfort from variations of different magnitudes and locations across the body, but instead this technique provides a new criteria through which environments with high degrees of radiant asymmetry can be compared.

We argue that it would be useful to consider the “radiant heterogeneity” across the body using tools such as this simulation method or through scanning of the body and surrounding surface temperatures to better understand these more nuanced but potentially very significant influences on thermal comfort. Future work should consider how radiant heterogeneity might be incorporated into comfort models or used to reevaluate the conditions that may be created in a space. This should be considered for radiant systems design and wall insulation as well as for the development of shading systems and window design for direct solar inputs, and how the bouncing and reflecting of both longwave and shortwave radiation can create this heterogeneity.

This consideration of the variation across the body and its impact on comfort becomes problematic for the definition of MRT when considering local variation between convex surfaces of the body exchange between local body surfaces. MRT is defined as the average of a uniform theoretical “enclosure.” The inside of an arm has the largest part of its view factor, usually consisting of the body and not the enclosure. Assuming a uniform body temperature allows a net-zero exchange between body segments, but in reality, there is significant temperature variation across the body. This is another aspect that may have a significant impact on thermal sensation and comfort. The net Watts from each segment of the body would need to be calculated, including both enclosure and self-occluding body segments.

While we considered the body’s surface temperature in the MRT calculations, we did not calculate for every body segment how its varying emissivity due to clothing or skin exposure level may influence net Watts of radiative exchange at each point. In doing so the radiant emission from the surface also changes. This affects the net radiant flux between the irradiance received (as determined by the radiant temperature of the surroundings and used to describe the MRT in this study) and

the radiosity (the radiation emitted as determined by the surface temperature and reflected as determined by the emissivity). Again, the net watts need to be determined. This can be added to the simulation tools, and a surface temperature scanning system can be used to estimate surface temperature as well as emissivity and will be part of future work. In considering these challenges, we argue that abstracting the radiant heat component of thermal exchanges with the body into one temperature, like MRT, begins to break down as one begins to consider the full resolution of the highly geometric and variable components of radiant heat transfer to and from the body. Finally, it is the net Watts of heat gained or lost from the body by radiation that truly defines, and would best predict, the impact on thermal comfort. While temperature abstractions enable a more intuitive interpretation of hot or cold, they remain embedded in methods that systematically average out variations that we have shown can be significant. Future work should consider how either a shift toward real heat measurements or more resolved temperature factors can be used while still being accessible and interpretable for comfort models.

4.4. Importance of BSPRT for human thermo-physiology modeling

Body segment plane radiant temperature (BSPRT) can be used as input to human thermo-physiology models [49,54] that require the knowledge of the local environment around each body part to compute local skin temperature. Based on the local body temperature and mean skin temperature, a person’s local and overall thermal sensation can be projected by applying a local thermal comfort model such as by Zhang et al. [50]. Body parts that are exposed to solar radiation have a direct influence on skin temperature; other body parts are indirectly affected due to blood circulation transporting heat from the warm body parts to the cooler body parts.

Better prediction of the thermal comfort at human body parts is an emerging topic due to the transition of the built environment towards occupant-centric design and the necessity to describe the local environment around individuals better. In prior work on thermal comfort, a uniform radiant environment is assumed most of the time. When measurements of air and globe temperature at different heights in the vicinity of the occupants are available, they are used to estimate the MRT of each body part. However, such an approach, due to the limited measurements, fails to consider that different sides of the body part, as shown in our experiments, can be exposed to shortwave and longwave radiation to a different extent.

5. Conclusion

Experimenting in a test room with a subject exposed to radiant fluxes within the indoor environment shows how variations in both longwave and shortwave heat fluxes across space can result in widely varying MRX values. Variations of up to 14.5 °C across the room were identified, and these values were used within the PMV comfort model to determine that the thermal comfort of a person sitting in different parts of the room would vary widely, from −0.27 to 2.45, showing the possibility of mapping the entire radiant field rather than assuming one MRT value for a thermal zone. In comparison, the recommended range of PMV for comfort in an office space is −0.5 to 0.5, a much narrower range than shown in our study using new high-resolution methods. The majority of this variation results from the impact of solar radiation.

Furthermore, a ray-tracing technique to map the radiant heat fluxes upon a human body mesh provides a high-resolution mean radiant temperature (MRT) as well as examines the heterogeneity of radiant temperatures perceived across different regions of the body due to asymmetric radiant fluxes from multiple heat sources. It was found that in the scenario which includes solar exposure the radiant temperature across the body can vary by over 30 °C. This cannot be reflected by simply providing an MRT value, which averages all these values into a single mean temperature. Finally, these values were used as detailed

environmental inputs for a human thermo-physiological model that is capable of predicting skin temperature distribution over the whole body parts and consequently can project both overall and local thermal comfort based on the thermal sensation at different regions of the body. This work, therefore, provides a methodological advance in being able to resolve, understand and predict how radiant heat fluxes impact overall and local thermal comfort and thermal sensation.

Declaration of Competing Interest

The authors declare that they have no known competing financial interests or personal relationships that could have appeared to influence the work reported in this paper.

Data availability

Data will be made available on request.

Appendix A. Supplementary material

Supplementary data to this article can be found online at <https://doi.org/10.1016/j.enbuild.2023.113581>.

References

- [1] A. ASHRAE, Standard 55–2020: Thermal Environmental Conditions for Human Occupancy, American Society of Heating, Refrigerating, and Air-Conditioning Engineers, Inc., Atlanta, 2020.
- [2] McIntyre. (1972). McIntyre: Radiant temperature and thermal comfort—Google Scholar. https://scholar.google.com/scholar_lookup?title=Radiant%20temperature%20and%20thermal%20comfort&publication_year=1972&author=D.A.%20McIntyre&author=I.%20Griffiths#d=gs_cit&u=%2Fscholar%3Fq%3Dinfo%3AZBKqKGC84EJ%3Ascholar.google.com%2F%26output%3Dcite%26scirp%3D0%26hl%3Den.
- [3] E. Arens, D. Heizerling, G. Paliaga, Sunlight and indoor thermal comfort, *ASHRAE J.* 7 (2018) 12–21.
- [4] DeGreef, J. M., & Chapman, K. S. (1998). Simplified thermal comfort evaluation of MRT gradients and power consumption predicted with the BCAP methodology. <https://www.osti.gov/biblio/649438>.
- [5] K.H. Yang, C.H. Su, An approach to building energy savings using the PMV index, *Build. Environ.* 32 (1) (1997) 25–30, [https://doi.org/10.1016/S0360-1323\(96\)00027-3](https://doi.org/10.1016/S0360-1323(96)00027-3).
- [6] A. Standard, Standard 55–2017 Thermal Environmental Conditions for Human Occupancy, American Society of Heating, Refrigerating and Air Conditioning Engineers, Atlanta, GA, USA, 2017.
- [7] H. Zhang, E. Arens, C. Huizenga, T. Han, Thermal sensation and comfort models for non-uniform and transient environments, part II: Local comfort of individual body parts, *Build. Environ.* 45 (2) (2010) 389–398, <https://doi.org/10.1016/j.buildenv.2009.06.015>.
- [8] O. Kaynakli, U. Unver, M. Kilic, Evaluating thermal environments for sitting and standing posture, *Int. Commun. Heat Mass Transfer* 30 (8) (2003) 1179–1188, [https://doi.org/10.1016/S0735-1933\(03\)00183-0](https://doi.org/10.1016/S0735-1933(03)00183-0).
- [9] D.N. Sorensen, Radiation between segments of the seated human body, *Roomvent.* 2002 (1) (2002) 317–320.
- [10] I. Atmaca, O. Kaynakli, A. Yigit, Effects of radiant temperature on thermal comfort, *Build. Environ.* 42 (9) (2007) 3210–3220, <https://doi.org/10.1016/j.buildenv.2006.08.009>.
- [11] K. Katić, R. Li, W. Zeiler, Thermophysiological models and their applications: A review, *Build. Environ.* 106 (2016) 286–300.
- [12] P. Fanger, Radiation data for the human body, *ASHRAE Trans.* 76 (1970) 338–373.
- [13] P.O. Fanger, Thermal comfort. Analysis and applications in environmental engineering, *Thermal Comfort. Anal. Appl. Environ. Eng.* (1970).
- [14] D. Aviv, H. Guo, A. Middel, F. Meggers, Evaluating radiant heat in an outdoor urban environment: Resolving spatial and temporal variations with two sensing platforms and data-driven simulation, *Urban Clim.* 35 (2021), 100745, <https://doi.org/10.1016/j.uclim.2020.100745>.
- [15] T. Miyahara, W. Urabe, Y. Nakano, Simplified human body model for evaluating thermal radiant environment in a radiant cooled space, *Build. Environ.* 36 (7) (2001) 801–808.
- [16] M.H. Vorre, R.L. Jensen, J. Le Dréau, Radiation exchange between persons and surfaces for building energy simulations, *Energ. Buildings* 101 (2015) 110–121.
- [17] F. Meggers, A. Kim, S. Rucevicz, C. Merchant, K. Chen, E. Teitelbaum, Improving mean radiant temperatures sensing using multidirectional non-contacting temperature sensors to avoid convective errors with globe thermometers, *Proceed. IEEE MetroLivEnv* 5 (2022). <https://www.metrolivenv.org/>.
- [18] E. Teitelbaum, H. Alsaad, D. Aviv, A. Kim, C. Voelker, F. Meggers, J. Pantelic, Addressing a systematic error correcting for free and mixed convection when measuring mean radiant temperature with globe thermometers, *Sci. Rep.* 12 (1) (2022) Article 1, <https://doi.org/10.1038/s41598-022-10172-5>.
- [19] E. Teitelbaum, K.W. Chen, F. Meggers, H. Guo, N. Houchois, J. Pantelic, A. Rysanek, Globe thermometer free convection error potentials, *Sci. Rep.* 10 (1) (2020) 1–13, <https://doi.org/10.1038/s41598-020-59441-1>.
- [20] Sofia Thorsson, Fredrik Lindberg, Ingegård Eliasson, Holmer Björn, Different methods for estimating the mean radiant temperature in an outdoor urban setting, *Int. J. Climatol.: J. R. Meteorol. Soc.* 27 (14) (2007) 1983–1993.
- [21] A. Handbook—Fundamentals, Physiological principles and thermal comfort, ASHRAE, Atlanta, 2021.
- [22] H. Guo, D. Aviv, M. Loyola, E. Teitelbaum, N. Houchois, F. Meggers, On the understanding of the mean radiant temperature within both the indoor and outdoor environment, a critical review, *Renew. Sustain. Energy Rev.* 117 (2020), 109207.
- [23] P.O. Fanger, B.M. Ipsen, G. Langkilde, B.W. Olesen, N.K. Christensen, S. Tanabe, Comfort limits for asymmetric thermal radiation, *Energ. Buildings* 8 (3) (1985) 225–236.
- [24] A. Middel, M. Huff, E.S. Krayenhoff, A. Udupa, F.A. Schneider, PanoMRT: Panoramic infrared thermography to model human thermal exposure and comfort, *Sci. Total Environ.* 859 (2023), 160301, <https://doi.org/10.1016/j.scitotenv.2022.160301>.
- [25] A. Middel, E.S. Krayenhoff, Micrometeorological determinants of pedestrian thermal exposure during record-breaking heat in Tempe, Arizona: Introducing the MaRTy observational platform, *Sci. Total Environ.* 687 (2019) 137–151, <https://doi.org/10.1016/j.scitotenv.2019.06.085>.
- [26] D.-S. Lee, J.-H. Jo, Application of IR camera and pyranometer for estimation of longwave and shortwave mean radiant temperatures at multiple locations, *Build. Environ.* 207 (2022), 108423, <https://doi.org/10.1016/j.buildenv.2021.108423>.
- [27] D.-S. Lee, E.-J. Kim, Y.-H. Cho, J.-W. Kang, J.-H. Jo, A field study on application of infrared thermography for estimating mean radiant temperatures in large stadiums, *Energ. Buildings* 202 (2019), 109360, <https://doi.org/10.1016/j.enbuild.2019.109360>.
- [28] C. Merchant, F. Meggers, M. Hou, D. Aviv, F.A. Schneider, A. Middel, Resolving radiant: combining spatially resolved longwave and shortwave measurements to improve the understanding of radiant heat flux reflections and heterogeneity, *Front. Sustain. Cities* 4 (2022), 869743, <https://doi.org/10.3389/frsc.2022.869743>.
- [29] Aviv, D. H. (2019). Thermal Reality Capture. ACADIA 19:UBIQUITY AND AUTONOMY [Proceedings of the 39th Annual Conference of the Association for Computer Aided Design in Architecture (ACADIA) ISBN 978-0-578-59179-7] (The University of Texas at Austin School of Architecture, Austin, Texas 21–26 October, 2019) Pp. 338–345. http://papers.cumincad.org/cgi-bin/works/paper/acadia19_338.
- [30] D. Aviv, J. Gros, H. Alsaad, E. Teitelbaum, C. Voelker, J. Pantelic, F. Meggers, A data-driven ray tracing simulation for mean radiant temperature and spatial variations in the indoor radiant field with experimental validation, *Energ. Buildings* 254 (2022), 111585, <https://doi.org/10.1016/j.enbuild.2021.111585>.
- [31] D. Aviv, M. Hou, E. Teitelbaum, F. Meggers, Simulating invisible light: A model for exploring radiant cooling's impact on the human body using ray tracing, *Simulation* (2022), 00375497221115735.
- [32] Aviv, D., Teitelbaum, E., Kvochick, T., Bradford, K., & Meggers, F. (2019). Generation and Simulation of Indoor Thermal Gradients: MRT for Asymmetric Radiant Heat Fluxes. Proceedings of Building Simulation 2019. Building Simulation, Rome, Italy.
- [33] T. Hoyt, CBE MRT tool: Online user guide [JavaScript], Original work published 2014, CenterForTheBuiltEnvironment. (2016), <https://github.com/CenterForTheBuiltEnvironment/mrt>.
- [34] M. La Gennusa, A. Nucara, G. Rizzo, G. Scaccianocce, The calculation of the mean radiant temperature of a subject exposed to the solar radiation—A generalised algorithm, *Build. Environ.* 40 (3) (2005) 367–375, <https://doi.org/10.1016/j.buildenv.2004.06.019>.
- [35] E. Arens, T. Hoyt, X. Zhou, L. Huang, H. Zhang, S. Schiavon, Modeling the comfort effects of short-wave solar radiation indoors, *Build. Environ.* 88 (2015) 3–9, <https://doi.org/10.1016/j.buildenv.2014.09.004>.
- [36] W.H. Chiang, C.Y. Wang, J.S. Huang, Evaluation of cooling ceiling and mechanical ventilation systems on thermal comfort using CFD study in an office for subtropical region, *Build. Environ.* 48 (2012) 113–127.
- [37] Y. Khan, V.R. Khare, J. Mathur, M. Bhandari, Performance evaluation of radiant cooling system integrated with air system under different operational strategies, *Energy Build.* 97 (2015) 118–128.
- [38] Y.L. Yin, R.Z. Wang, X.Q. Zhai, T.F. Ishugah, Experimental investigation on the heat transfer performance and water condensation phenomenon of radiant cooling panels, *Build. Environ.* 71 (2014) 15–23.
- [39] G.M. Revel, M. Arnesano, F. Pietroni, Development and validation of a low-cost infrared measurement system for real-time monitoring of indoor thermal comfort, *Meas. Sci. Technol.* 25 (8) (2014), 085101, <https://doi.org/10.1088/0957-0233/25/8/085101>.
- [40] M. Rahiminejad, D. Khovaly, Experimental study of the hydrodynamic and thermal performance of ventilated wall structures, *Build. Environ.* 233 (2023), 110114.
- [41] E. Teitelbaum, H. Guo, J. Read, F. Meggers, Mapping Comfort with the SMART (Spherical Motion Average Radiant Temperature) Sensor, in: Proceedings of the 15th IBPSA Conference, 2017, August 7. http://www.ibpsa.org/proceedings/BS2017/BS2017_644.pdf.
- [42] S. Kotthaus, T.E.L. Smith, M.J. Wooster, C.S.B. Grimmond, Derivation of an urban materials spectral library through emittance and reflectance spectroscopy, *ISPRS J.*

- Photogramm. Remote Sens. 94 (2014) 194–212, <https://doi.org/10.1016/j.isprsjprs.2014.05.005>.
- [43] G. Rizzo, G. Franzitta, G. Cannistraro, Algorithms for the calculation of the mean projected area factors of seated and standing persons, *Energ. Buildings* 17 (3) (1991) 221–230.
- [44] M. Hou, J. Pantelic, D. Aviv, Spatial analysis of the impact of UVGI technology in occupied rooms using ray-tracing simulation, *Indoor Air* 31 (5) (2021) 1625–1638.
- [45] Ward, G. J. (1994). The RADIANCE lighting simulation and rendering system. 459–472.
- [46] F. Tartarini, S. Schiavon, pythermalcomfort: A Python package for thermal comfort research, *SoftwareX* 12 (2020), 100578, <https://doi.org/10.1016/j.softx.2020.100578>.
- [47] EN ISO 7730. (2005). Ergonomics of the thermal environment Analytical determination and interpretation of thermal comfort using calculation of the PMV and PPD indices and local thermal comfort criteria. Standard International Organization for Standardization, 3(605), e615.
- [48] E. Arens, H. Zhang, C. Huizenga, Partial-and whole-body thermal sensation and comfort—Part II: Non-uniform environmental conditions, *J. Therm. Biol* 31 (1–2) (2006) 60–66.
- [49] Y. Takahashi, A. Nomoto, S. Yoda, R. Hisayama, M. Ogata, Y. Ozeki, S. Tanabe, Thermoregulation model JOS-3 with new open source code, *Energ. Buildings* 231 (2021), 110575, <https://doi.org/10.1016/j.enbuild.2020.110575>.
- [50] H. Zhang, E. Arens, C. Huizenga, T. Han, Thermal sensation and comfort models for non-uniform and transient environments: Part I: Local sensation of individual body parts, *Build. Environ.* 45 (2) (2010) 380–388.
- [51] EN ISO 7726. (2001). Ergonomics of The Thermal Environments: Instruments for measuring physical quantities. Standard International Organization for Standardization.
- [52] R. Daghighi, N. Adam, K. Sopian, B. Sahari, Thermal comfort of an air-conditioned office through different windows-door opening arrangements, *Build. Serv. Eng. Res. Technol.* 30 (1) (2009) 49–63, <https://doi.org/10.1177/0143624408099448>.
- [53] M. Charai, O. Horma, A. Mezrhab, M.A. Moussaoui, Passive heating in thermally compliant office building: Validated and simulated scenarios, *Fuel Commun.* 9 (2021), 100026, <https://doi.org/10.1016/j.jfueco.2021.100026>.
- [54] M. Fu, W. Weng, W. Chen, N. Luo, Review on modeling heat transfer and thermoregulatory responses in human body, *J. Therm. Biol* 62 (2016) 189–200.